TU/e

Eindhoven University of Technology
Faculty of Electrical Engineering
Division of Telecommunication Technology and Electromagnetics
Electro-Optical Communications Group

Semiconductor Micro-ring Laser Model for All-optical Signal Processing Applications

By D. Moreno Domínguez

Master of Science Thesis
carried out from October 2007 to July 2008

Supervisors:
Dr. J. Herrera Llorente
Asist. Prof. E. Tangdiongga

Graduation professor:
Prof. H. J. S. Dorren

/faculteit elektrotechniek

Technische Universiteit Eindhoven

Faculty of Electrical and Electronic Engineering

Telecommunication Technology and Electromagnetics (TTE)

Electro-Optical Communications (ECO)

Master of Science Thesis

Semiconductor Micro-ring Laser Model for All-optical Signal Processing Applications

By

David Moreno Domínguez

Supervisors:
Dr. J. Herrera Llorente
Asist. Prof. E. Tangdiongga

Graduation professor:
Prof. H. J. S. Dorren

Eindhoven, 2008

Summary

As the bit-rate per wavelength channel and the number of channels steadily keep increasing in telecommunication networks due to the development of optical transmission technologies, switching still is experiencing the limitations of electronics. It is expected that the great mismatch between the transmission bandwidth and the switching capacity may be overcome by the development of photonic technologies. All-optical signal processing in photonic devices, including wavelength conversion, logic gates, signal regeneration, optical memories, etc., are key issues that have to be address in order to realize all optical switching in photonic devices.

Semiconductor micro-ring lasers are very promising devices for all-optical signal processing as they are very compact, relatively easy to fabricate, show power efficiency and have high wavelength selectivity. It is therefore very important to evaluate the performance of these devices, by means of numerical models for the micro-ring lasers in order to understand their behavior in several all-optical signal processing configurations, especially when the interacting pulse duration becomes very short as expected for very high operation bit-rates.

To investigate the performance of micro-ring based all-optical signal processing systems, a comprehensive model as close to the physical world as possible, has been developed for this thesis, which includes both inter- and intra-band ultra-fast carrier dynamics, broadband noise and gain dispersion effects. In the proposed model the lasing modes directly arise from the ring-laser boundary conditions applied, and their power is controlled by the gain dispersion.

After the model has been completed, two main targets have been evaluated along this thesis: evaluate if the recovery time of the micro-ring laser is fast enough for high-speed signal processing and therefore if it can beat the performance of alternative SOA-based devices.

To carry out these objectives, firstly a 300 and 30 μm ring lasers are characterized and the results qualitatively compared with experimental data gathered from a 2 mm ring-laser. Secondly, the response of a single 30 μm ring-laser operating as a wavelength converter is studied for input signals of 2.5, 10 and 40 Gb/s and its performance is tested.

Relaxation oscillation phenomena has been found to be the most limiting factor in the performance of these devices for signal processing applications at high bit-rates. This performance can be improved only to a certain limit by increasing the bias current. Also, pulse energy must be carefully selected to avoid recovery delays due to gain saturation or even laser shut-off.

Contents

Chapter 1

Introduction

1.1. Towards optical switching

Since year 2000 global network traffic is dominated by internet (IP) data, and has suffered a steady increase in demand with traffic growths close to 100% each year [1].This constant need for higher bandwidth has been met thanks to the progress in optical fiber backbone networks, whose transport speed has been pushed by a factor of 10 every seven years [2]. Single-wavelength capacity has evolved in the last years from 2.5 Gb/s to 10 Gb/s, and systems with 40 Gb/s are already being commercially deployed in the field.

However, network performance does not depend on transmission capacity only. A communication network basically has two functionalities: transmission and switching [3]. The information is sent to a final destination through transmission channels via many intermediate network nodes. It is at these nodes where the switching takes place, routing the bits from the origin to the destination along a prescribed pathway. Though the backbone network transmission has moved to the optical domain to take advantage of the optic fiber huge capacity, so far switching is still done in the electrical domain. Electrical switching is very efficient and the technology is mature, and the combination of optical transmission and electrical switching works very well. The switching in the electrical domain, however, is experiencing more and more pressure from the above-mentioned ever-increasing transmission capacity. The situation becomes even worse when there are many wavelength channels in one optical fiber, as is common in today's WDM networks, because a large number of optical receivers, modulators and lasers will be required at each network nodes, resulting in a prohibitively expensive network. At the same time, high-capacity electrical signal processing consumes relatively large space and high power. The state-of-the-art CRS-1 router from CISCO, with up to 92 Tb/s switch capacity, occupies 100m2 space, consumes 1 MW power and weighs 60 Ton [4].

To alleviate this problem, switching in the optical domain is being the subject of intensive research. The possibility of monolithic integration of the optical switch fabric, keeping the high-speed data in the optical domain and eliminating unnecessary optical-electrical-optical conversion, allows lower power consumption, smaller real estate, and reduced cost [5]. The ultimate goal of optical switching is to achieve optical packet switching (OPS). The idea is that at each node, optical data packets are switched individually: when an optical packet arrives, the node will process the header information and then switch the packet to its destination based on the current resource availability. This means that the node should be reconfigured on a time scale shorter than the packet duration, which would be at this point already in the order of nanoseconds. Fig 1.1 shows the structure of a typical OPS node
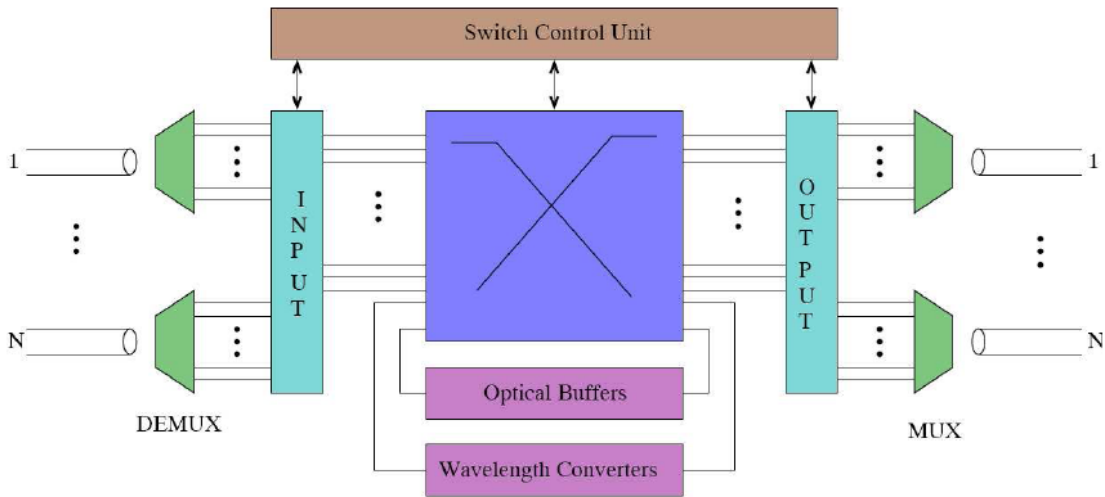
Figure 1.1: Schematic of a typical OPS node.

It is straightforward that many advanced all-optical signal processing functions are needed in an OPS node: all-optical header recognition, buffers, switching, wavelength conversion, flip-flop memories, logic gates, etc [6].

The key to success regarding to integration in photonics is the reduction of all this variety of functionalities to a few elementary components. One such solution being researched consists of 3 elementary devices: A passive waveguide structure for low-loss interconnection of devices and realization of miniaturized components like couplers, filters and multiplexers; an element for manipulating the phase of optical signals and an element for manipulating the amplitude of optical signals [7]. Large scale photonic

integrated circuits (PICs) using this scheme have already started to be commercially fabricated [8].

1.2. SOA-based technologies

Semiconductor material is very attractive in all-optical signal processing. Most efforts are centered in semiconductor optical amplifier (SOA)-based devices. SOAs have several striking advantages. Firstly, due to the gain of the device and strong resonate nonlinear effects, the optical power of the input signal can be very low, leading to high power efficiency. Secondly, the device dimension is small compared to devices based on other material and it has compact size of a few milimeters [9, 10].

A variety of different all-optical processing functions have already been successfully implemented using SOAs, such as all-optical flip-flops and wavelength converters [11]; and the European IST-LASAGNE project aims at designing and implementing the first modular, scalable and truly all-optical photonic router capable of operating at 40 Gb/s using this technology [12].

Inside the Eindhoven University of Technology Electro-optical Communications team (ECO) where this thesis has been developed, SOAs have been the subject of extensive modeling work and experimental research: a SOA numerical model considering ultrafast gain dynamics has been developed [13]; modeling of 160 Gb/s wavelength conversion, using a single SOA and an optical bandpass filter was realized and later experimentally demonstrated [14, 15]; and optical wavelength conversion at 320 Gb/s and all-optical packet switching using SOA based flip-flops at 160 Gb/s has been experimentally studied [16, 17], to mention some examples.

However, SOAs relatively long carrier lifetimes (typically tens to hundreds of picoseconds) result in significant pattern effects limiting the maximum pattern-effect-free bit rate [18], and their dimensions and power consumption makes them unsuitable for the levels of integration and miniaturization we see today in electronic-based technologies.

1.3.   Next step: micro-ring lasers

Micro-ring lasers have appeared as a promising approach for low-power nonlinear integrated photonic devices. Their small cavity volume, cleavage-free cavities, excellent wavelength selectivity and ultralow threshold, have arisen great interest. On top of that, their shorter recovery time, lower power consumption and much smaller size make them an interesting option to replace SOAs as key active element in large scale photonic integration.

Some progress has already been made in this field: a low-power optical memory based on coupled micro-ring lasers has been proposed and demonstrated [19], Though most of the applications and characterization work is being carried out with ring lasers of mm size [20, 21].

In short, micro-ring lasers are very promising in all-optical signal processing and are being explored for novel functions. It is therefore very important to understand the underlying physics, based on which the devices can be optimized and novel device concepts can be proposed

1.4.   Motivation of the work

Numerical modeling is always necessary to understand the working principle of the devices and to optimize their performance. It is also useful to verify a novel idea before implementing it in the lab. Although quite some work in this sense has already been done to study SOAs, to the best of our knowledge no comprehensive model of a micro-ring laser has yet been carried out. It is therefore very interesting to develop a micro-ring laser model within the context of ultra-high speed all-optical signal processing and to investigate the working principles numerically. With the knowledge gained from these numerical experiments, new insight can be generated to understand and optimize the all-optical signal processing systems better. At the same time, novel concepts for all-optical signal processing can be developed.

1.5. Objectives

The following questions arise when considering the micro-ring laser for all-optical signal processing: Is it fast enough for high speed signal processing? Can it beat SOA (and elecronics) performance?

To answer those in this thesis a series of objectives are set:

- Develop a model for the micro-ring laser as close to the physical world as possible: taking into account ultrafast carrier dynamics; using a broadband noise source; ring laser boundary conditions and a simple approximation for gain dispersion. This model with an example of the developed simulator outputs is explained in Chapter 2.

- Evaluate the validity of the model and if possible compare results with experimental laboratory data. This is done through characterization of 300 and 30 μm ring lasers, and experimental data is obtained from a 2 mm long laser. Results are shown in Chapter 3.

- Test applications using the model and check the performance of the micro-ring based solution. In Chapter 4, wavelength conversion on a single micro-ring laser is investigated. Evolution of the relaxation oscillation frequency, recovery time and rise-time for different bias and external pulse energies is studied, and performance for 2.5 Gb/s, 10 Gb/s and 40 Gb/s signals is analyzed

- Finally, conclusions are drawn is Chapter 5, where recommendations for future research are also proposed.

Chapter 2

Micro-ring laser numerical model

2.1. Introduction

As stated in the previous chapter, SOAs play an important role in optical communication systems and are very attractive for all-optical signal processing due to their large nonlinearity and power efficiency. However, SOAs are bulky and may not be suitable for operation at high bit-rates. Semiconductor micro-ring lasers might be an alternative device to overcome these limitations. Therefore it is necessary to perform numerical simulations based on well-grounded physical models to propose new ideas and to optimize the device (system) performance. In this chapter, the model used in this thesis is described in detail.

2.2. Active region model

2.2.1. SOA overview

A laser consists of a medium with optical gain, in which new photons are generated under positive feedback, making possible light amplification. The positive feedback is typically achieved through reflective mirrors creating an optical cavity. A source to supply energy to the gain medium is needed as well.

In a semiconductor laser the gain is provided by the active region. The active region of a semiconductor laser works in a very similar fashion as an SOA, a device that has been deeply studied and modeled. SOAs have reduced feedback and therefore are operated under their large bias threshold value, but the principles and equations that characterize their dynamics are essentially the same. Thus, the SOA model used for the active region will be firstly presented. After that, the necessary modifications to adapt the SOA model to a laser will be described.

An SOA is an optoelectronic device that under normal operation conditions can amplify an input light signal. It consists of a semiconductor active section, buried and surrounded by a lower refractive index material thus becoming a wave-guide. Under positive electrical current injection, the electrical carriers in the active region are in the population inversion state, allowing amplification of an external optical field via stimulated emission and therefore providing gain for the incoming signal. A schematic diagram of an SOA is shown in Figure 2.1.
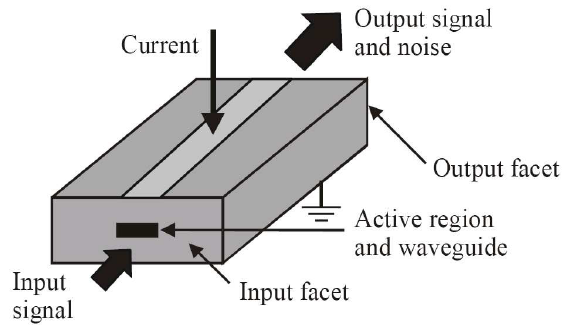

Figure 2.1: schematic of an SOA. [22]

The SOA gain strongly depends on the carrier density in the active region and is determined by the device characteristics, the optical signal injected and the electrical current bias. The gain is dramatically affected when the carrier density is modulated by either the bias current or an injected optical signal. Gain dynamics and carrier dynamics are the core of SOA modeling, along with the optical field propagation through the waveguide.

The most accurate way of modeling an SOA is to solve the Semiconductor Bloch Equation (SBE) but this is extremely time-consuming [23]. A simplified approach is to phenomenologically include the different physical processes, as is done in rate-equation models, which are very successful in explaining the experimental results for these devices. Also, for simplicity, polarization effects have been neglected and thus only one polarization is treated.

2.2.2. Basic model

The carrier dynamics are usually taken into account through the total carrier density N, its typical time evolution equation being the following:

$$\frac{\partial N}{\partial t} = \frac{\eta_i I}{qV} - \frac{N}{\tau_n} - v_g g S \qquad (2.2.1)$$

The first term accounts for carrier generation through the injection current, where I represents the bias current injected to the device, q is the electron charge, V is the volume of the waveguide and η_i is the internal quantum efficiency (for simplicity $\eta_i=1$).

The second term accounts for carrier spontaneous recombination, either radiative or non-radiative, being τ_n the carrier lifetime. This carrier life-time is in fact dependent on the carrier density through a quadratic equation [24], but this dependence can be neglected under the normal operating conditions of the device and is generally taken as a constant.

The last term accounts for the carriers being depleted via stimulated recombination, where v_g is the group velocity of the traveling optical field, g is the material gain and S is the total photon density coupled to the active region in both possible directions. The photon density is directly proportional to the optical power and they are linked by the formula:

$$P = h v_0 \sigma v_g S \qquad (2.2.2)$$

where h is the Planck constant, v_0 is the central optical frequency and σ is the modal cross section, which for a waveguide of a width w and a thickness d is defined as:

$$\sigma = \frac{wd}{\Gamma} \qquad (2.2.3)$$

The material gain g can be usually approximated to the total carrier density N through a linear relationship [25].

$$g = \frac{a}{v_g}\left(N - N_0\right) \qquad (2.2.4)$$

The parameter a is called the material gain coefficient and N_0 is the transparency carrier density (the carrier density level at which the material gain becomes zero and thus "transparent" to incoming light).

To complete this first basic model of the SOA, the propagation of the optical field across the active material section may be modeled via the propagation equation of a slow-varying complex envelope A:

$$\frac{\partial A^+}{\partial z} = \left(\frac{1+j\alpha_N}{2} \Gamma g - \frac{1}{2}\alpha_{int} \right) A^+ \qquad (2.2.5a)$$

$$\frac{\partial A^-}{\partial z} = \left(\frac{1+j\alpha_N}{2} \Gamma g - \frac{1}{2}\alpha_{int} \right) A^- \qquad (2.2.5b)$$

The +/- upperindex refer to the field propagating in either positive or negative direction, Γ is the confinement factor (the fraction of light traveling through the optically coupled region), a_N is the phase modulation factor and α_{int} is the internal loss coefficient. The first term in the right-hand side represents the amplification of the incoming optical field and the corresponding phase modulation associated with gain evolution (a_N, also called linewidth enhancement factor, determines how much the phase of the optical field is affected by variations in the gain, and therefore it is related to the lasing modes spectral width). The second term represents the loss that the optical field encounters while advancing through the waveguide due to material absorption.

As seen from the equation the complex envelope propagates in the z direction with an overall gain that depends on different terms. The group-velocity term has been removed from the analysis introducing the variable change $\tau=t-z/v_g$, and hereafter the time coordinate refers to a frame moving at the group velocity.

Finally, the complex envelope can be decomposed in optical power P and phase φ as shown below:

$$A = \sqrt{P} \cdot e^{j\phi} \qquad (2.2.6)$$

2.2.3. Extended model for ultrafast dynamics

As the main objective of this model is to investigate if the micro-ring semiconductor laser is suitable for ultrafast all-optical signal processing, it must provide accurate predictions in the picosecond and sub-picosecond time scales.

In order to model pulse propagation in an SOA under these regimes, it is necessary model the intra-band carrier dynamics so that the gain dynamics can be derived correctly. The gain can no longer be considered as dependent on the total carrier density, as only a local "pocket" of the total carriers are actually optically coupled,

therefore a new time evolution equation will be introduced for the carrier density in the optically coupled region. In fact, as will be seen later, a different equation for each band is needed.

Also, to achieve a good accuracy at such small time scales, several physical processes which have been neglected in the previous model have to be taken into account, being the most important two-photon absorption (TPA) and free-carrier absorption (FCA). In TPA, two photons are absorbed simultaneously, introducing additional loss to the incoming optical signal while exciting the carriers to a very high energy state. Similar to TPA, in FCA a photon is absorbed exciting a carrier to a higher energy state in the same band, introducing also additional loss to the input optical signal. These two phenomena combined accurately describe the carrier heating and spectral hole burning effects observed in practice [26, 27]. The extended field propagation equations are

$$\frac{\partial A^+}{\partial z} = \left(\frac{1+j\alpha_N}{2} \Gamma g - \frac{1}{2}\alpha_{int} - \frac{1+j\alpha_2}{2} \cdot \frac{\Gamma_2 \beta_2 P_t}{\sigma} - \frac{1}{2}\Gamma \beta_c n_c - \frac{1}{2}\Gamma \beta_v n_v \right) A^+ \quad (2.2.7a)$$

$$\frac{\partial A^-}{\partial z} = \left(\frac{1+j\alpha_N}{2} \Gamma g - \frac{1}{2}\alpha_{int} - \frac{1+j\alpha_2}{2} \cdot \frac{\Gamma_2 \beta_2 P_t}{\sigma} - \frac{1}{2}\Gamma \beta_c n_c - \frac{1}{2}\Gamma \beta_v n_v \right) A^- \quad (2.2.7b)$$

The third term on the right hand of the equation corresponds to the TPA and α_2, Γ_2 and β_2 respectively refer to the coefficient, confinement factor and phase modulation factor related to TPA. Pt is the total optical power which, neglecting ultrafast grating effects, is found as

$$P_t = \left| A_{cw} \right|^2 + \left| A_{ccw} \right|^2 \quad (2.2.8)$$

The fourth and fifth terms correspond to the FCA in the conduction and valence bands, where β_c and β_v refer to the FCA coupling coefficients and n_c and n_v are the carrier densities in the optically coupled region in each band.

As mentioned before, the gain expression considered now depends on the local carrier densities at the conduction and valence bands:

$$g = \frac{a}{v_g} \left(n_c + n_v - N_0 \right) \quad (2.2.9)$$

The evolution of the carrier densities in the optically coupled region can be obtained from the rate equations below:

$$\frac{\partial n_c}{\partial t} = -\frac{n_c - \bar{n}_c}{\tau_{1c}} - g v_g S - \beta_c n_c v_g S \quad (2.2.10a)$$

$$\frac{\partial n_v}{\partial t} = -\frac{n_v - \overline{n}_v}{\tau_{1v}} - g v_g S - \beta_v n_v v_g S \qquad (2.2.10b)$$

Here $\overline{n}_c$ and $\overline{n}_v$ refer to the quasi-equilibrium values for the local carrier densities in the conduction and the valence bands, and τ_{1c} and τ_{1v} are the carrier to carrier scattering times. The terms in the right side of the equation correspond to the relaxation to the quasi-equilibrium values due to carrier to carrier interactions, the stimulated emission and the FCA, as this last excites carriers in the optically coupled pocket to a higher energy state out of it. The quasi-equilibrium values are dynamically changing and may be determined as:

$$\overline{n}_c = N_0 f\left(E_{fc}, T_c, E_c\right) \qquad (2.2.11a)$$

$$\overline{n}_v = N_0 f\left(E_{fv}, T_v, E_v\right) \qquad (2.2.11b)$$

where $E_{fc/v}$ denote the quasi-fermi energy levels, $T_{c/v}$ the band temperatures and $E_{c/v}$ are the transition energies in each band. Here f is the Fermi-Dirac distribution function:

$$f\left(E_f, T, E\right) = \frac{1}{1 + \exp\left(\dfrac{E - E_f}{k_B T}\right)} \qquad (2.2.12)$$

The value for the transparency carrier density may be obtained from:

$$N_{0c/v} = \int_{\hbar\omega_0 - \frac{\hbar}{2\tau_2}}^{\hbar\omega_0 + \frac{\hbar}{2\tau_2}} \frac{1}{2\pi^2} \left[\frac{2m_{c/v}^*}{\hbar^2}\right]^{3/2} E^{1/2} dE \qquad (2.2.13)$$

though in this model the parameter value is taken from literature [28].

The calculation of the energy levels and temperatures is a must to determine the local carrier density evolution. They may be consistently computed from the total carrier and energy densities in both the conduction and valence bands, using:

$$N = \frac{1}{V} \sum_k f\left(E_{fc}, T_c, \frac{\hbar^2 k^2}{2m_c^*}\right) \qquad (2.2.14a)$$

$$N = \frac{1}{V} \sum_k f\left(E_{fv}, T_v, \frac{\hbar^2 k^2}{2m_v^*}\right) \qquad (2.2.14b)$$

$$U_c = \frac{1}{V} \sum_k \frac{\hbar^2 k^2}{2m_c^*} f\left(E_{fc}, T_c, \frac{\hbar^2 k^2}{2m_c^*}\right) \qquad (2.2.15a)$$

$$U_v = \frac{1}{V} \sum_k \frac{\hbar^2 k^2}{2m_v^*} f\left(E_{fv}, T_v, \frac{\hbar^2 k^2}{2m_v^*}\right) \qquad (2.2.15b)$$

being $\hbar$ the Dirac constant, V the volume of the active region in the SOA, k the wave vector of the electron wave function, m^*_c the effective mass of the electrons around the bottom of the conduction band, and m^*_v the effective mass of the electrons around the peak of the valence band.

N is the total carrier density, equal for both bands, and $U_{c/v}$ denote the energy density in the conduction and valence bands.

The total carrier density satisfies the following rate equation:

$$\frac{\partial N}{\partial t} = \frac{\eta_i I}{qV} - \frac{N}{\tau_n} - v_g gS + \frac{\Gamma_2}{\Gamma}(\beta_2 h v_0 v_g)v_g S^2 \tag{2.2.16}$$

The terms in the right side of the equation correspond to the carrier injection, the spontaneous recombination, the stimulated emission amplification and the TPA, the presence of the latest being explained by its generation of new carriers via exciting electrons from the valence band into the conduction band. Notice that TPA does not appear in the local carrier densities rate equations, as the electron-hole pairs generated have high energies and are out of the optically coupled region.

The energy densities satisfy the following rate equations:

$$\frac{\partial U_c}{\partial t} = -\frac{U_c - \bar{U}_c}{\tau_{hc}} + h v_0 \beta_c n_c v_g S - E_c g v_g S + E_{2c} \frac{\Gamma_2}{\Gamma}(\beta_2 h v_0 v_g)v_g S^2 \tag{2.2.17a}$$

$$\frac{\partial U_v}{\partial t} = -\frac{U_v - \bar{U}_v}{\tau_{hv}} + h v_0 \beta_v n_v v_g S - E_v g v_g S + E_{2v} \frac{\Gamma_2}{\Gamma}(\beta_2 h v_0 v_g)v_g S^2 \tag{2.2.17b}$$

where τ_{hc} and τ_{hv} are the time constants for the heated carriers in the conduction and valence bands to relax to the lattice temperature, also known as carrier-phonon relaxation time, and $\bar{U}_c$ and $\bar{U}_v$ denote the equilibrium values for the energy densities.

In the right side of the equation the terms describe the relaxation to the equilibrium values due to carrier-phonon scattering or carrier cooling, the FCA, the stimulated emission and the TPA.

Finally, the equilibrium values for the energy densities, that are where the carriers have the same temperature as the lattice (T_L), may be obtained as:

$$\bar{U}_c = \frac{1}{V}\sum_k \frac{\hbar^2 k^2}{2m^*_c} f\left(E_{fc}, T_L, \frac{\hbar^2 k^2}{2m^*_c}\right) \tag{2.2.18a}$$

$$\overline{U_v} = \frac{1}{V} \sum_k \frac{\hbar^2 k^2}{2m_v^*} f\left(E_{fv}, T_L, \frac{\hbar^2 k^2}{2m_v^*} \right) \tag{2.2.18b}$$

2.3. ASE noise

Most of the semiconductor laser models reported in the literature predict the wavelengths of the allowed modes in the laser cavity and then proceed solve the rate equations for each one of those modes, applying certain weights to each frequency [29, 30]. In those models, the effect of spontaneous emission noise required to generate the lasing condition is usually included by adding a constant value to the optical field propagation equation, modeling the amount of noise power coupled to the mode. Therefore, this noise has a virtually zero bandwidth; it is allocated only in the lasing modes frequencies and shows a non-stochastic behavior.

In this thesis, a model of the broadband spontaneous emission noise has been implemented including its stochastic nature., This way the same rate equations applied to a single mode are valid for the whole spectrum of the simulation. It is also unnecessary to previously calculate which modes will be allowed in the cavity, being built up by themselves when adding the proper boundary conditions, which will be the subject of the next section. Therefore, the proposed semiconductor laser model uses a Montecarlo approach.

The origin of the noise fluctuations in the SOA lie within the quantum nature of the amplification process itself. Fluctuations affecting the intensity and the phase of the signal arise from the amplified spontaneous emission (ASE). Also fluctuations in the carrier density are present due to the discrete nature of recombination processes, called shot noise. Within the analysis based on rate and propagation equations, the spontaneous emission noise is incorporated by adding a Langevin noise source to the propagation equation:

$$\frac{\partial A^+}{\partial z} = \left(\frac{1 + j\alpha_N}{2} \Gamma g - \frac{1}{2} \alpha_{\text{int}} - \frac{1 + j\alpha_2}{2} \cdot \frac{\Gamma_2 \beta_2 P_t}{\sigma} - \frac{1}{2} \Gamma \beta_c n_c - \frac{1}{2} \Gamma \beta_v n_v \right) A^+ + A_{sp}^{+} \tag{2.3.1a}$$

$$\frac{\partial A^-}{\partial z} = \left(\frac{1 + j\alpha_N}{2} \Gamma g - \frac{1}{2} \alpha_{\text{int}} - \frac{1 + j\alpha_2}{2} \cdot \frac{\Gamma_2 \beta_2 P_t}{\sigma} - \frac{1}{2} \Gamma \beta_c n_c - \frac{1}{2} \Gamma \beta_v n_v \right) A^- + A_{sp}^{-} \tag{2.3.1b}$$

The effects of the shot noise are typically weaker and are neglected in the model hereafter. In the presence of these noise sources, the fields become random and the equations stochastic.

Some assumptions are taken to model the noise. This solution relies in the physical origin of the spontaneous emission noise, that is, a fraction of the photons generated by the spontaneous recombination term is coupled into the optical waveguide and amplified. The generation rate of these spontaneous photons may be modeled as:

$$R_{sp} = \beta_{sp} \frac{N}{\tau_n} \qquad (2.3.2)$$

where β_{sp} is named the spontaneous emission coefficient, and determines the fraction of spontaneously generated photons that are coupled into the waveguide.

To consider the noisy nature of these photons it is assumed that this generation rate is related to the statistical characteristics of a random process, that is mean and variance. Due to the discrete nature of the carriers and the relatively low value of this rate, a Poissonian distribution has been found to be the most suitable approach for it.

For the phase noise, utterly required to have a fully random field term, the best guess is to consider a uniform distributed noise.

Therefore the contribution of the amplified spontaneous emission noise to the optical field is:

$$A_{sp} = \begin{cases} S_{sp} = Pois(\lambda_{sp} \propto R_{sp}) \\ \phi_{sp} = U(0, 2\pi) \end{cases} \qquad (2.3.3)$$

2.4.   Laser configuration

So far the model reported is valid for an SOA. However by applying the required boundary conditions it can be easily transformed into a semiconductor laser model, specifically a ring laser in this case.

Semiconductor ring lasers consist of a circular active waveguide or "ring" coupled with straight or bend waveguide which may be passive or active. An electron microscopy image of a ring laser is shown in Figure 2.2. The ring is pumped with an injection current above threshold operation providing the optical gain. When the optical

field travels through the whole circumference, a fraction of the light is coupled out into the output waveguide whereas the rest remains within the ring. This works as a resonant cavity providing positive feedback and building up only those modes whose frequency is a multiple of the free spectral range (FSR) defined as follows:

$$FSR = \frac{c}{n_r L} \qquad (2.4.1)$$

where c is the speed of light and n_r and L are the effective refractive index and circumference of the circular active waveguide, respectively. It should be stressed that in the proposed model this condition will not be imposed to the modes, but naturally arises from the stochastic noise when the boundary conditions are applied.
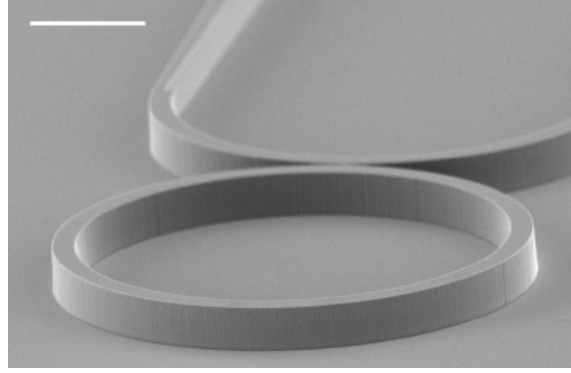

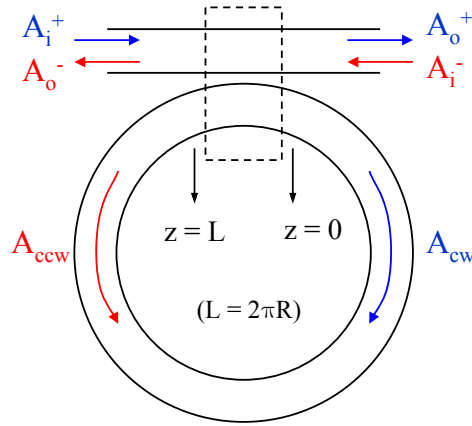*Figure 2.2: an electron microscopy image of a ring laser. [31].*

Figure 2.3: schematic of a ring laser.

A schematic diagram of a ring laser is shown in Fig 2.3. Unlike in the Fabry-Perot lasers, the optical fields traveling in opposite directions in the ring lasers are practically independent, though they influence each other indirectly by their effects in the material gain (which is the same for both) via the total carrier density. However, optical coupling

between the modes occurs due to small reflections in the coupler or imperfections in the waveguide, typically with reflectivity values lower than 10^{-3}.

Hereafter, the optical fields advancing in each direction of the ring shall be denoted as A_{cw} and A_{ccw} which stand for clockwise and counter-clockwise directions.

A simple 2x2 coupler has been used to model the coupling between the ring and the waveguide. The basic coupling matrix for these devices is shown below:

$$\overbrace{\begin{matrix} A_{i1} \rightarrow & \\ A_{i2} \rightarrow & \end{matrix} \boxed{\alpha_c} \begin{matrix} \rightarrow A_{o1} \\ \rightarrow A_{o2} \end{matrix}}^{\text{Coupler}}$$

$$\begin{bmatrix} A_{o1} \\ A_{o2} \end{bmatrix} = \begin{bmatrix} \sqrt{1-\alpha_c} & j\sqrt{\alpha_c} \\ j\sqrt{\alpha_c} & \sqrt{1-\alpha_c} \end{bmatrix} \begin{bmatrix} A_{i1} \\ A_{i2} \end{bmatrix} \tag{2.4.2}$$

Taking into account that the coupler works in both directions (for clockwise and counter-clockwise) and adding reflections in the coupler inputs, the final energy-conservative coupling matrix used in the model as boundary condition is:

$$\tag{2.4.3}$$

$$\begin{bmatrix} A_{o,cw} \\ A_{cw(z=0)} \\ A_{o,ccw} \\ A_{ccw(z=L)} \end{bmatrix} = \begin{bmatrix} \sqrt{(1-\alpha_c)} & j\sqrt{\alpha_c(1-R)} & 0 & 0 \\ j\sqrt{\alpha_c} & \sqrt{(1-\alpha_c)(1-R)} & 0 & \sqrt{R} \\ 0 & 0 & \sqrt{(1-\alpha_c)} & j\sqrt{\alpha_c(1-R)} \\ 0 & \sqrt{R} & j\sqrt{\alpha_c} & \sqrt{(1-\alpha_c)(1-R)} \end{bmatrix} \begin{bmatrix} A_{i,cw} \\ A_{cw(z=L)} \\ A_{i,ccw} \\ A_{ccw(z=0)} \end{bmatrix}$$

Here α_c is the coupling factor between the ring and the waveguide and R models the reflections that couple the counter-propagating modes. It can be noticed that reflections have only been applied to the ring-side inputs of the coupler, as reflections for external injection are not relevant for the model.

2.5. Gain dispersion

In the model described so far, the gain is assumed to be independent of the wavelength. This may be an accurate assumption when dealing with signals larger than 10 ps and relatively narrow optical bandwidths. However, if the pulses become shorter than 10 ps [32] and especially when including broadband ASE noise, which basically is distributed among the whole available spectrum, gain dispersion has to be considered.

The gain spectrum is approximated by a parabolic profile. The carrier dynamics remain unchanged while the field propagation equation with gain dispersion effects becomes [33].

$$\frac{\partial A_{cw}}{\partial z} + g_2 \frac{\partial^2 A_{cw}}{\partial t^2} = f(A_{cw}) + A_{sp} \qquad (2.5.1a)$$

$$\frac{\partial A_{ccw}}{\partial z} + g_2 \frac{\partial^2 A_{ccw}}{\partial t^2} = f(A_{ccw}) + A_{sp} \qquad (2.5.1b)$$

$$f(A_x) = \left(\frac{1 + j\alpha_N}{2} \Gamma g - \frac{1}{2} \alpha_{int} - \frac{1 + j\alpha_2}{2} \cdot \frac{\Gamma_2 \beta_2 P_t}{\sigma} - \frac{1}{2} \Gamma \beta_c n_c - \frac{1}{2} \Gamma \beta_v n_v \right) A_x \quad (2.5.1c)$$

The g_2 parameter is defined as the second order derivative of the gain:

$$g_2 = \left. \frac{\partial^2 g}{\partial \omega^2} \right|_{\omega = \omega_0} \qquad (2.5.2)$$

Typical dispersion models also consider a g_1 term related to the carrier density, modeling the peak wavelength dependence with the optical and electrical pumping conditions. However, for simplicity we consider a parabola centered in the central wavelength and determined by its spectral width. That is, the first-order dispersion parameter is zero:

$$g_1 = \left. \frac{\partial g}{\partial \omega} \right|_{\omega = \omega_0} \simeq 0 \qquad (2.5.3)$$

2.6. Numerical implementation

2.6.1. Carrier rate equations

To take into account the longitudinal dependence of the carrier densities, band temperatures, Fermi energy levels, etc., the laser is divided into many small sections as shown in Figure 2.4. In each small section, these physical variables are assumed to be constant along the longitudinal axis and the set of differential equations of the model, Eqs. (2.2.9) to (2.2.11) and (2.2.14) to (2.2.18), with the exception of the field propagation equation, can be readily solved in each section as ordinary differential equations (ODEs) [34].
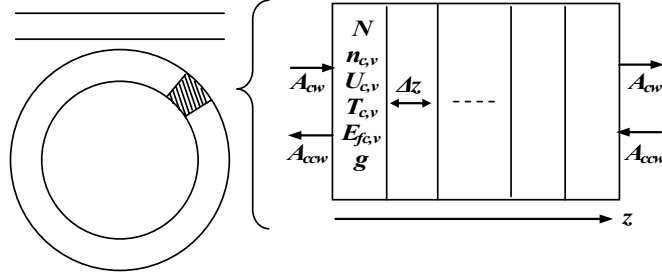
Figure 2.4: schematic diagram of the ring laser, divided into longitudinal sections.

The Euler rule method is used because of its simplicity. The low accuracy of this method may be controlled increasing the sampling frequency in time or the number of sections in space, which are linked by the expression $\Delta z = v_g \Delta t$. The Euler rule for the total carrier density equation (2.2.16) becomes:

$$N(z, t + \Delta t) = N(z, t) + dN(z, t) \cdot \Delta t \qquad (2.6.1)$$

The local carrier densities and the energy densities, Eqs. (2.2.10) and (2.2.17), can be solved using the same method as for the total carrier density

2.6.2. Field propagation

For the case of the field propagation equations, it may be stated that each step in space requires an update in time because of the group-velocity term that has been eliminated in the analysis. If neither the noise nor the gain dispersion are considered (Eq. (2.2.7)), the field equations can be readily solved as ODEs:

$$A_{cw}(z + \Delta z, t + \Delta t) = A_{cw}(z, t) + dA_{cw}(z, t) \cdot \Delta z \qquad (2.6.2a)$$

$$A_{ccw}(z + \Delta z, t + \Delta t) = A_{ccw}(z, t) + dA_{ccw}(z, t) \cdot \Delta z \qquad (2.6.2b)$$

To include the effects of the noise, the Euler rule has to be modified to include the spontaneous emission noise field term, as follows:

$$A_{cw}(z + \Delta z, t + \Delta t) = A_{cw}(z, t) + dA_{cw}(z, t) \cdot \Delta z + A_{sp,cw} \qquad (2.6.3a)$$

$$A_{ccw}(z + \Delta z, t + \Delta t) = A_{ccw}(z, t) + dA_{ccw}(z, t) \cdot \Delta z + A_{sp,ccw} \qquad (2.6.3b)$$

The power of the noise field term is generated using a Poisson distribution for the number of photons, whose mean (and standard deviation) is:

$$\lambda_{sp} = R_{sp} w d \Delta z \Delta t \tag{2.6.4}$$

being R_{sp} the spontaneous photon generation rate seen in Eq. (2.3.2).

As mentioned in a previous sub-chapter, the phase of the noise field term is generated using a uniform distribution between 0 and 2π.

When the gain dispersion effect is included, the field equation becomes a second-order nonlinear differential equation. It should be noticed that using fast Fourier transformation to introduce the time derivative is quite difficult to implement, if not impossible, due to the time-dependence of the other variables in the model. The second-order time derivative is replaced with a centered finite difference approximation, becoming:

$$\frac{\partial^2 A(z,t)}{\partial t^2} = \frac{A(z,t+\Delta t) - 2A(z,t) + A(z,t-\Delta t)}{\Delta t^2} \tag{2.6.5}$$

Using this, the fields can be solved:

$$A_{cw}(z+\Delta z, t+\Delta t) = h_a A_{cw}(z,t) + h_b A_{cw}(z,t-\Delta t) + h_c f(A_{cw}) + A_{sp,cw} \tag{2.6.6a}$$

$$A_{cw}(z+\Delta z, t+\Delta t) = h_a A_{cw}(z,t) + h_b A_{cw}(z,t-\Delta t) + h_c f(A_{cw}) + A_{sp,cw} \tag{2.6.6b}$$

where $f(A_x)$ is the function stated in Eq. (2.5.1c). The propagation constants may be calculated as:

$$h_a = \frac{\Delta t^2 - 2g_2\Delta z}{\Delta t^2 - g_2\Delta z} \tag{2.6.7a}$$

$$h_b = \frac{g_2\Delta z}{\Delta t^2 - g_2\Delta z} \tag{2.6.7b}$$

$$h_c = \frac{\Delta t^2\Delta z}{\Delta t^2 - g_2\Delta z} \tag{2.6.7c}$$

It can be seen in Eq. (2.6.6) that to obtain the field at the next time-step, the values for the field in the present and previous time-steps are needed.

2.6.3. Band equations

One of the most time-consuming parts in solving the carrier equations is to evaluate the carrier temperatures T_c, T_v and the Fermi-energy levels E_{fc}, E_{fv} with the knowledge of the total carrier density N and the total energy densities U_c, Uv through Eqs. (2.2.14) to

(2.2.17). The summations over k can be approximated by Fermi integrations, resulting in the equations for the conduction band:

$$N = \frac{2}{\sqrt{\pi}} \left(\frac{2\pi m_c^*}{h^2} \right)^{3/2} (k_B T_c)^{3/2} \int_0^\infty \frac{\varepsilon_c^{1/2}}{1+\exp\left(\varepsilon_c - \varepsilon_{fc}\right)} d\varepsilon \qquad (2.6.8a)$$

$$N = \frac{2}{\sqrt{\pi}} \left(\frac{2\pi m_v^*}{h^2} \right)^{3/2} (k_B T_v)^{3/2} \int_0^\infty \frac{\varepsilon_v^{1/2}}{1+\exp\left(\varepsilon_v - \varepsilon_{fv}\right)} d\varepsilon \qquad (2.6.8b)$$

$$U_c = \frac{2}{\sqrt{\pi}} \left(\frac{2\pi m_c^*}{h^2} \right)^{3/2} (k_B T_c)^{5/2} \int_0^\infty \frac{\varepsilon_c^{3/2}}{1+\exp\left(\varepsilon_c - \varepsilon_{fc}\right)} d\varepsilon \qquad (2.6.9a)$$

$$U_v = \frac{2}{\sqrt{\pi}} \left(\frac{2\pi m_v^*}{h^2} \right)^{3/2} (k_B T_v)^{5/2} \int_0^\infty \frac{\varepsilon_v^{3/2}}{1+\exp\left(\varepsilon_v - \varepsilon_{fv}\right)} d\varepsilon \qquad (2.6.9b)$$

where k_B is the Boltzmann constant and ε denotes normalized energy levels: $\varepsilon = \dfrac{E}{k_B T}$

The Fermi integrations can be accurately solved by an analytical approximation [35], resulting two pairs of nonlinear equations. To obtain the solutions E_{fc}, E_{fv} and T_c, T_v for a given set of N, U_c and U_v a searching algorithm is employed. Due to the nonlinearities of the equations, accurate solution is not easily obtained.

In practice, Newton-Rapson's finite differences method is used. This method successively finds better approximations to the roots of a real valued function by taking an initial guess, approximating the function by its tangent line and then computing the x-intercept, iterating until a certain tolerance range is achieved.

When the temperature is equal to the lattice temperature T_L, only the Fermi energy must be found. Its value is obtained iterating: $E_{n+1}=E_n+\Delta E$, where:

$$\Delta E = 2h_E \frac{N_{sol} - N(E_n)}{N(E_n + h_E) - N(E_n - h_E)} \qquad (2.6.10)$$

N_{sol} is the value of the carrier density at the looked-for solution, which is known, and h_E is the energy step considered to approximate the tangent

When both the Fermi energy levels and the temperatures must be obtained, the following set of equations is to be solved:

$$\begin{bmatrix} N_{sol} - N(E_n, T_n) \\ U_{sol} - U(E_n, T_n) \end{bmatrix} = \begin{bmatrix} \dfrac{\partial N(E_n, T_n)}{\partial E} & \dfrac{\partial N(E_n, T_n)}{\partial T} \\ \dfrac{\partial U(E_n, T_n)}{\partial E} & \dfrac{\partial U(E_n, T_n)}{\partial T} \end{bmatrix} \begin{bmatrix} \Delta E \\ \Delta U \end{bmatrix} \qquad (2.6.11)$$

where

$$\frac{\partial f\left(x_n, y_n\right)}{\partial x} = \partial f_x = \frac{f(x_n + h_x, y_n) - f(x_n - h_x, y_n)}{2h_x} \qquad (2.6.12)$$

Similarly to the previous case, N_{sol} and U_{sol} are the total carrier and energy densities values at the desired pair of solutions and h_T and h_E the temperature and Fermi energy steps considered to approximate the tangents. Substituting Eq (2.6.12) in Eq (2.6.11) and operating we arrive to the final expressions:

$$\Delta E = 2h_E \frac{\partial U_T \cdot (N_{sol} - N) - \partial N_T \cdot (U_{sol} - U)}{\partial U_T \cdot \partial N_E - \partial N_T \cdot \partial U_E} \qquad (2.6.13a)$$

$$\Delta T = 2h_T \frac{dU_E \cdot (N_{sol} - N) - dN_E \cdot (U_{sol} - U)}{dU_E \cdot dN_T - dN_E \cdot dU_T} \qquad (2.6.13b)$$

2.7. Model parameters

2.7.1. Physical constants

- q [C]   : Electron charge $= 1.60217646 \cdot 10^{-19}$ C
- m_e [Kg]   : Electron mass $= 9.10938188 \cdot 10^{-31}$ Kg
- h [J·s]   : Planck constant $= 6.62606896 \cdot 10^{-34}$ J·s
- k_B [J/K]   : Boltzmann constant $= 8.617343 \cdot 10^{-5}$ eV/K
- c [m/s]   : Speed of light $= 3 \cdot 10^{-8}$ m/s
- eV [J]   : Electronvolt $= 1.60217646 \cdot 10^{-19}$ J

2.7.2. Parameters

- f_s [Hz]   : Simulation sampling frequency $= 40.96$ THz
- λ [m]   : Reference wavelength $= 1.55$ μm
- L [m]   : Ring laser circumference $= 30$ μm
- w [m]   : Active layer width $= 2$ μm
- d [m]   : Active layer thickness $= 0.2$ μm
- m^*_c [kg]   : Carrier effective mass (c. band) $= 0.046\, m_e$
- m^*_v [kg]   : Carrier effective mass (v. band) $= 0.45\, m_e$
- E_c [J]   : Conduction band transition energy $= 0.03$ eV
- E_v [J]   : Valence band transition energy $= 0.7$ eV
- E_{2c} [J]   : Conduction band transition energy for TPA $= 0.003$ eV

- E_{2v} [J]   : Valence band transition energy for TPA   = 0.07 eV
- T_L [K]   : Lattice temperature   = 300 K
- N_0 [m^{-3}]   : Transparency carrier density.   = $1.6 \cdot 10^6$ μm^{-3}
- η_i [-]   : Internal quantum efficiency   = 1
- n_r [-]   : Material refractive index   = 3
- I [A]   : Injected current   = 100 mA
- Γ [-]   : Confinement factor   = 0.2
- τ_n [s]   : Carrier lifetime   = 200 ps
- τ_{hc} [s]   : Carrier-phonon relaxation time (c. band)   = 0.7 ps
- τ_{hv} [s]   : Carrier-phonon relaxation time (v. band)   = 0.25 ps
- τ_{lc} [s]   : Carrier-carrier scattering time (c. band)   = 0.1 ps
- τ_{lv} [s]   : Carrier-carrier scattering time (v. band)   = 0.05 ps
- a [m^3/s]   : Material gain coefficient   = $2.4 \cdot 10^{-6}$ μm^3/ps
- g_2 [s^2/m]   : Second order gain term   = $36 \cdot 10^{-6}$ ps^2/μm
- α_{int} [m^{-1}]   : Material loss coefficient   = $4 \cdot 10^{-3}$ μm^{-1}
- α_N [-]   : Phase modulation factor   = 7
- β_c [m^2]   : FCA coupling coefficient (c. band)   = $0.1 \cdot 10^{-8}$ μm^2
- β_v [m^2]   : FCA coupling coefficient (v. band)   = 0.0 μm^2
- β_2 [m/W]   : TPA coefficient   = $3.5 \cdot 10^{-10}$ m/W
- Γ_2 [-]   : TPA confinement factor   = 0.5
- α_2 [-]   : TPA phase modulation factor   = 1.5
- β_{sp} [-]   : Spontaneous emission coefficient   = $5 \cdot 10^{-5}$
- α_c [-]   : Waveguide-Ring coupling factor   = 0.2
- R [-]   : Waveguide-Ring reflection factor   = 10^{-4}

2.8. Simulator overview

The ring laser numerical model described so far has been implemented into a program that simulates the operation of the device since the instant a constant bias current is applied to it, being possible to study the effects of external optical injection once the steady state is achieved.

The simulator operates keeping a vector for each of the variables N, T_c, T_v, E_{fc}, E_{fv}, n_c, n_v $\overline{n_c}$, $\overline{n_v}$, U_c, U_v, $\overline{U_c}$ and $\overline{U_v}$, containing their values for each section at a given instant of time. For subsequent time-steps the vector is updated with new values. In the case of

the optical field, three complex vectors are used: one for the present time, one to obtain the values in the next iteration, and one for the previous time-step, as it is needed to solve Eq. (2.6.6).

The simulation runs going through three main stages:

- Firstly, the solution for the rest state is obtained, that is, the values for the active region variables without optical injection. Band temperatures are equal to the lattice temperature T_L, the optical field vectors are all set to zero, and the carrier equations are solved supposing there is no variation in time.

- Secondly the simulator runs till a steady state is achieved. In each time-step the field vector is first propagated, using the carrier temperature and energy values obtained in the last iteration and the field values for the next time-step are calculated, its input coming from the spontaneous noise as there is no external injection in this stage. Then, the rest of the variables are updated using the field values obtained at the last iteration. At the boundary sections, the coupling condition is also applied in each time-step obtaining the clockwise and counter clockwise outputs.

- Finally, if required, gain dynamics may be studied by introducing external optical injection. This stage operates exactly as the previous one, but this time the input signal introduced via the coupling condition may have non-zero values.

Several files are created to store the data generated by the simulator, this data files can be plotted using MATLAB. Displayed in Figs 2.5 to 2.8 are the outputs of a simulation example reaching the steady state and using the parameter values shown in the previous section. For the three dimensional curves, it should be remembered that the sections in z=0 and z=30μm are connected, as it is a ring, it is there also where the coupling with the waveguide occurs

It can be seen in Fig 2.5a how the total carrier density rapidly decreases as the carriers are depleted via stimulated emission, corresponding with an output power peak in Fig 2.7. As the carrier densities in the optically coupled regions (Fig 2.5b and Fig 2.5c) decrease, the gain also decreases and so does the output power; this gives time for the carrier numbers to rebuild and so the gain raises again, continuing this relaxation oscillation until a steady state is achieved. The rest of the variables also follow a similar relaxation oscillation process.
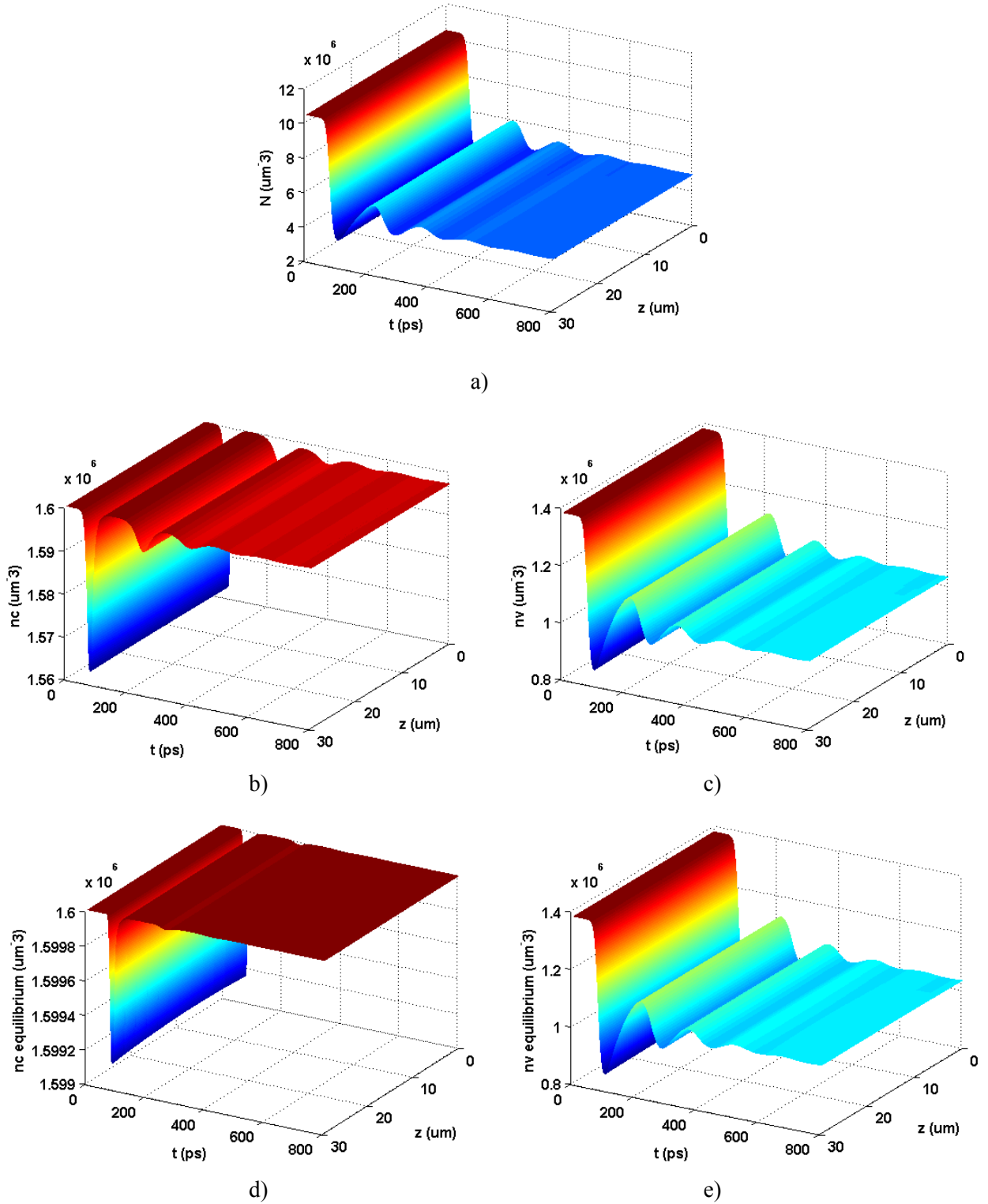
a)

b)

c)

d)

e)

Figure 2.5: ·3D MATLAB plotting of the outputs of an example simulation. a) Total carrier density, b) and c) local carrier density in the optically coupled region for the conduction and valence bands, d) and e) local carrier densities in the optically coupled region when in the equilibrium state for the conduction and valence bands
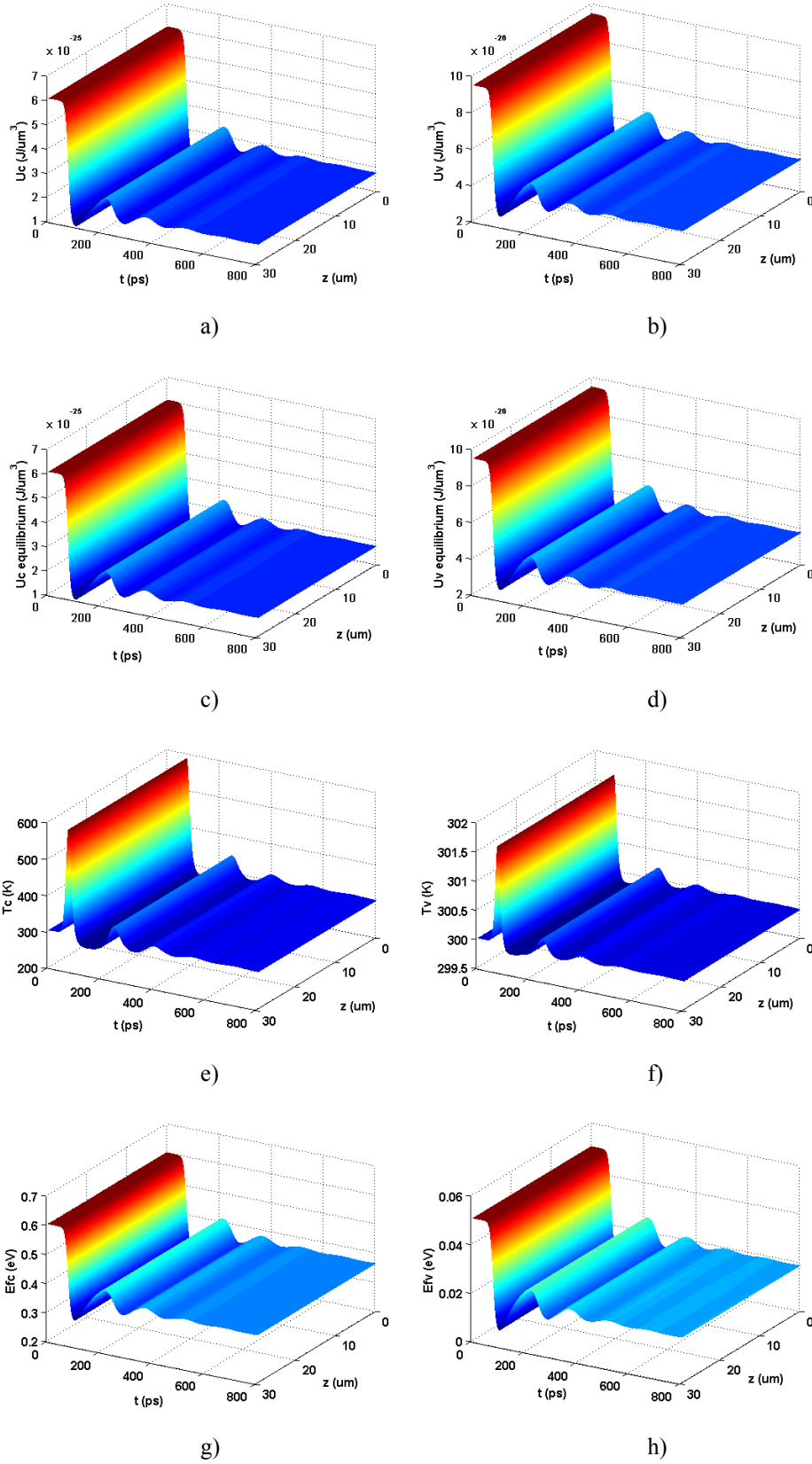
Figure 2.6: ·3D MATLAB plotting of the outputs of an example simulation. a) and b) energy densities for c. and v. bands, c) and d) energy densities when in equilibrium for c. and v. bands, e) and f) band temperature for c. and v. bands, g) and h) Fermi energy levels for c. and v. bands.

The simulator also has several built-in post processing functions to help to the analysis of the results. The spectrum of the signals can be computed and plotted as shown in Figure 2.7 where the main mode can be seen at 1550 and the adjacent resonant frequencies at 1530 and 1575 nm, though the last two are heavily suppressed due to the gain dispersion and gain competition effect. The signal can also be filtered in the frequency domain and its signal recovered which is the output displayed in Figure 2.8. Other utilities will be introduced in the next chapters for characterization of the device and study of the gain dynamics.
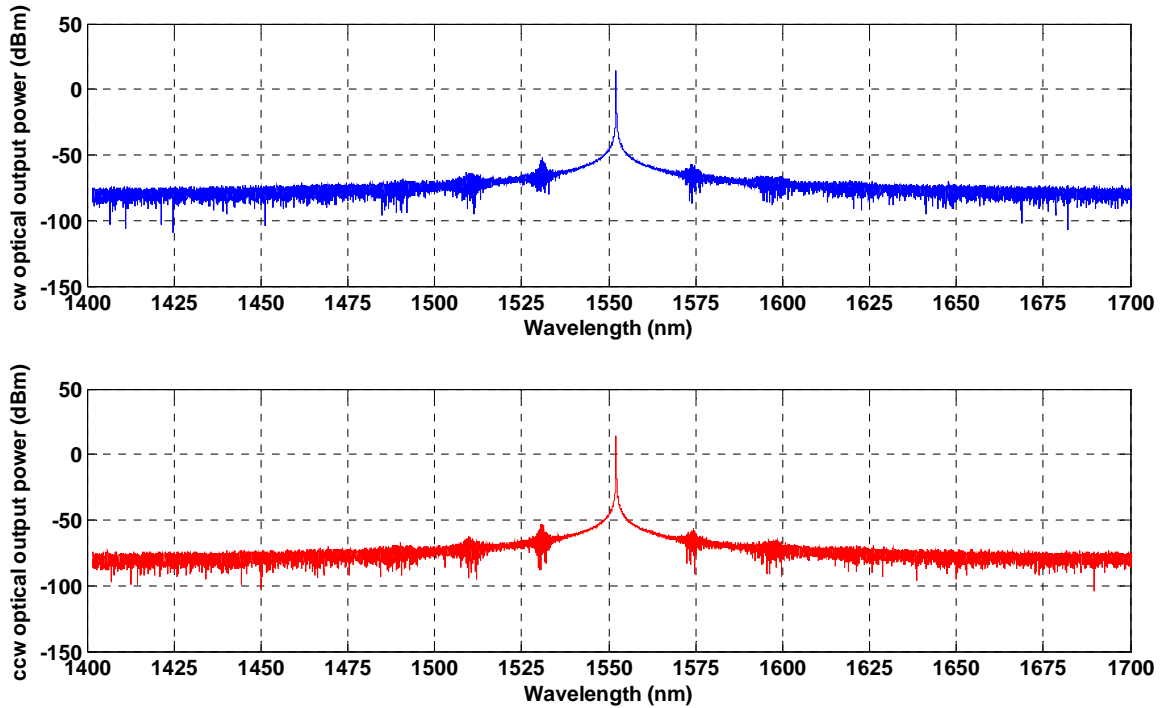
Figure 2.7: plot of the output powers in frequency domain for an example simulation, the f axis has been transformed to a wavelength axis.
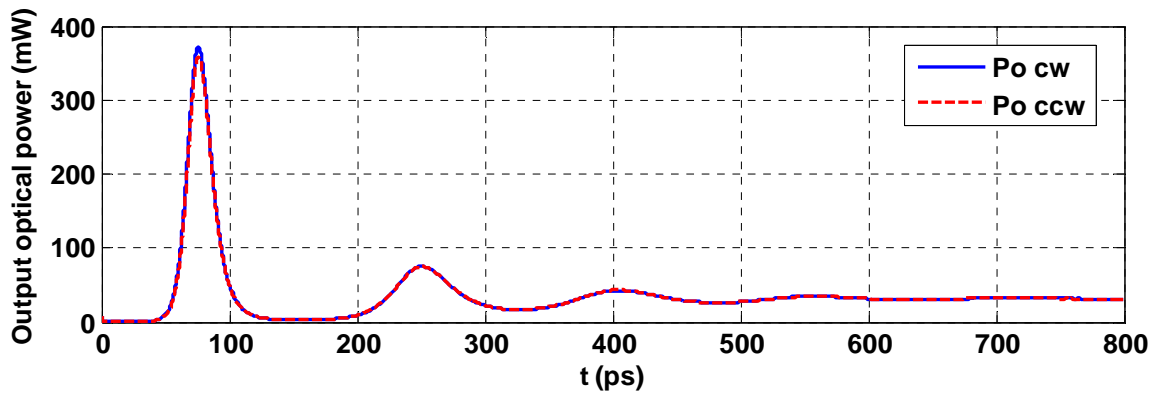
Figure 2.8: plot of the output powers in time domain for an example simulation, the main mode has been previously filtered in frequency domain with a raised cosine filter.

Chapter 3

Characterization of 300 and 30 μm micro-ring lasers

3.1. Introduction

Before developing specific numerical experiments with the ring laser, several characterization studies must me carried out in order to evaluate the model performance. And whenever possible, comparison with experimental laboratory results should be made. This thesis target is the study of small size micro-ring lasers (in the order of 10 micron circumference), as fast dynamics properties are foreseen. However, due to the lack of actual devices with such reduced sizes and because currently available devices are rings in the order of millimeter circumference, two ring lasers of different sizes are characterized in this chapter: the study target of 30 μm circumference and a longer one of 300 μm. Larger order of magnitudes were not feasible to characterize due to long computational times and high volume of data outputs, as the ultrafast dynamics implementation require sampling frequency rates above 20 THz for the proper functioning of the model. In any case, and due to the relatively high difference in sizes only a qualitative comparison between simulation and experimental results may be done, without parameter adjustment.

3.2. Optical bandwidth

The device optical bandwidth is controlled by the gain dispersion parameter g_2 (Eq.2.5.2). In Figure 3.1, the effect of varying this parameter in a 30 μm ring over the output spectrum is shown.

As a general rule, the higher g_2, the narrower the device bandwidth. That is, for a zero value all the resonant modes in the available spectrum are lasing modes At the time this thesis is developed there was no experimental data available about the value of this parameter for micro-ring lasers. However, measuring the side-mode suppression for

different values of g_2, its relationship with the device bandwidth can be extracted. A suitable bandwidth, in accordance with the orders of magnitude reported in the literature [32], was selected at $g_2=3.6 \cdot 10^{-6}$ ps^2/ μm.
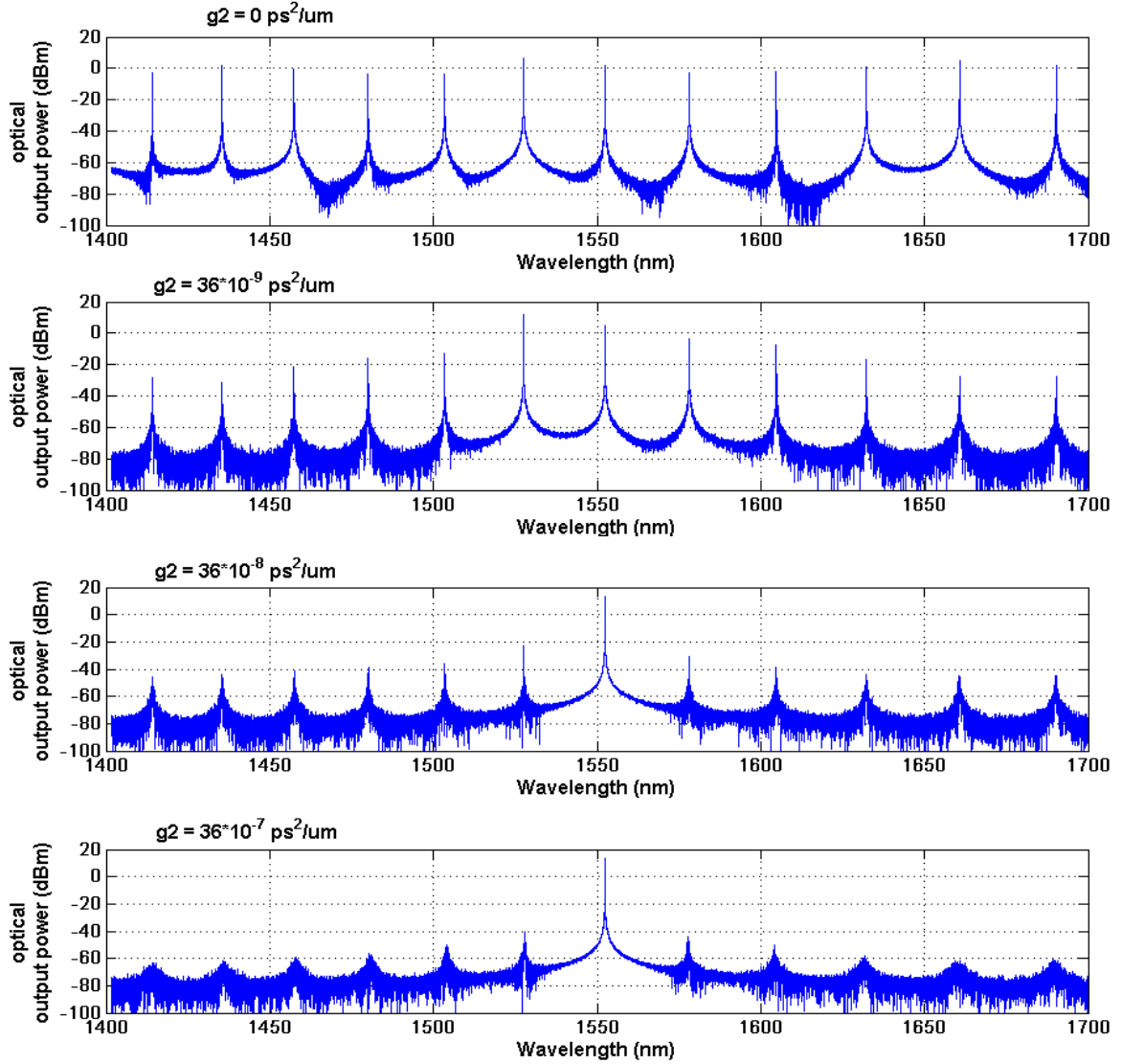

Figure 3.1: Effect on the optical spectrum of varying the gain dispersion parameter in a 30 μm ring

3.3.   Output signal study

A sample simulation trace is shown here for each ring, using the parameters mentioned in section 2.7 and varying only the ring length. The resulting output power of the clockwise and counter-clockwise directions is shown in Figures 3.2 to 3.5.

It can be seen that the total output power signal from the 300 μm ring (Figure 3.1a) shows strong oscillations in comparison to the smoother result from the 30 μm (Figure

3.3a). This is due to the fact that in the longer ring there are several modes competing for the material gain. Having a longer circumference means a lower FSR (Eq. 2.4.1) and the allowed modes being closer together. Therefore for the same optical bandwidth the longer ring will shown more modes. This is clearly observed in the frequency domain (Figures 3.4 and 3.5). In fact, the 30 μm ring shows such a large suppression of the first resonant frequencies (over 50 dB) that it can be considered as single-mode.
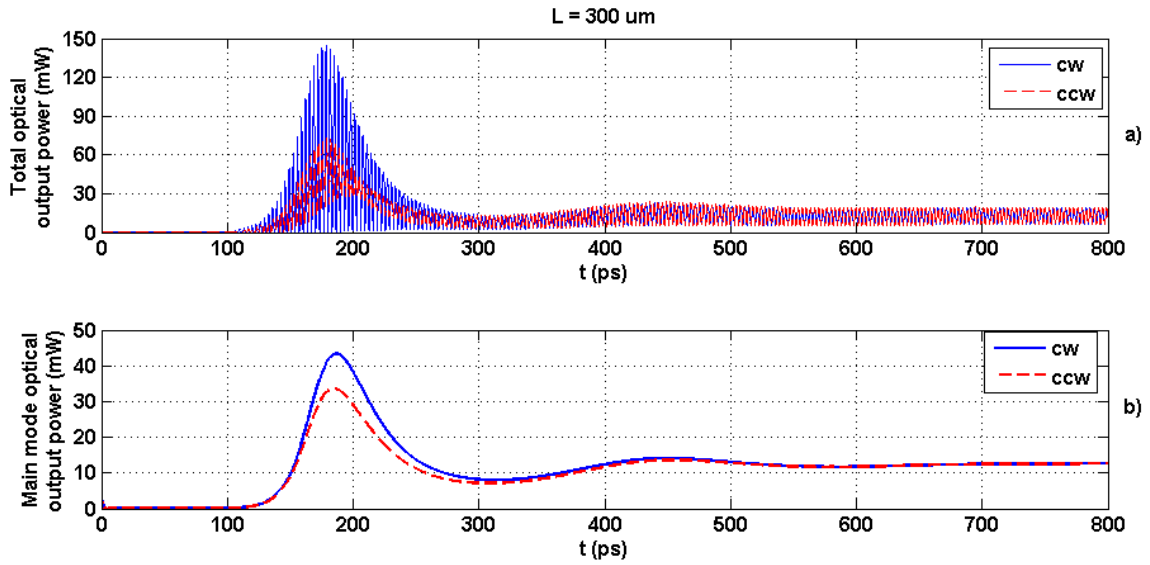
Figure 3.2: Output optical powers for a simulation of a 300 μm ring. a) Total power.b) Main mode power
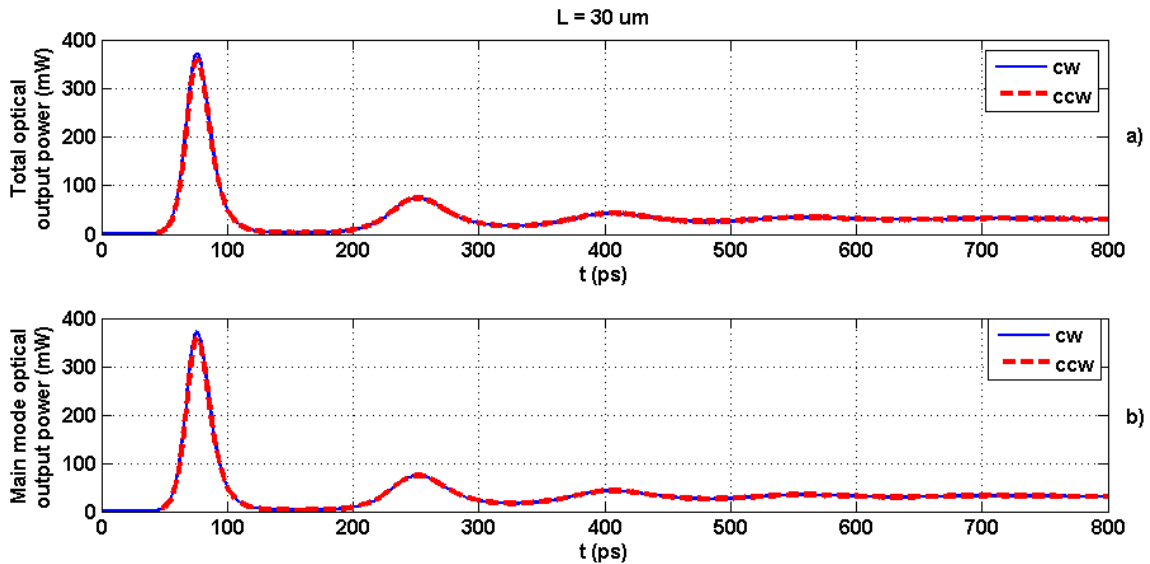
Figure 3.3: Output optical powers for a simulation of a 30 μm ring. a) Total power.b) Main mode power

The theoretical values of 0.33 THz and 3.33 THz for the FSRs of the 300 μm and 30 μm rings respectively match very well the simulated results. The slight mismatch can be

attributed to the correlation between phase, gain and power, which causes a chirp in the signal. This is also responsible for the central mode being located at a wavelength slightly different than the 1550 nm theoretical one.

The steady-state spectrum for the clockwise and counter clockwise output fields is exactly the same. This will hold for this model as long as there is no external optical injection.
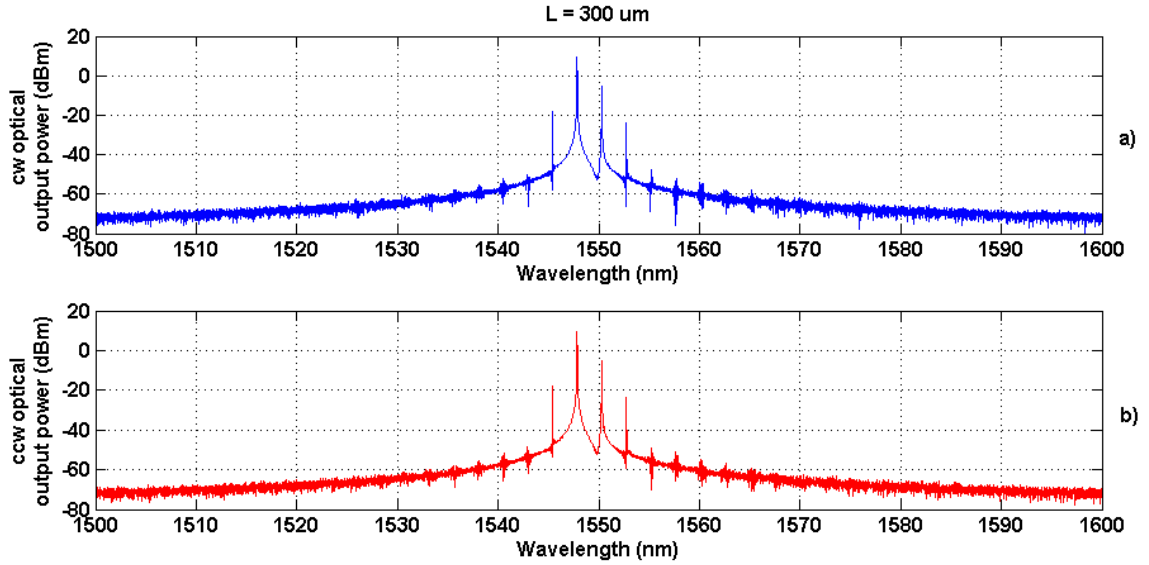
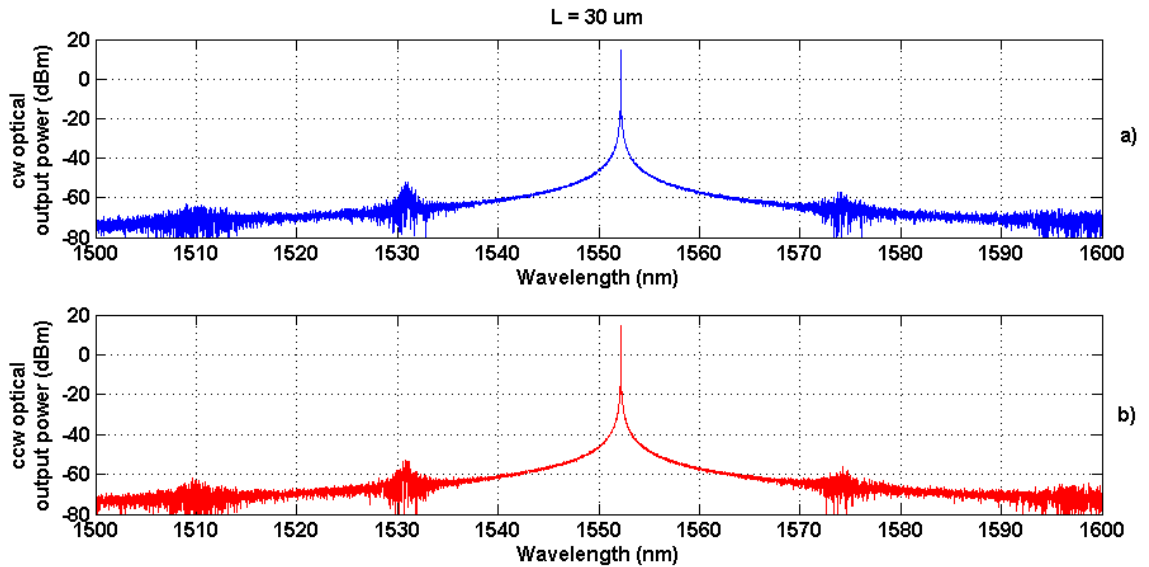

Figure 3.4: Output spectrum for a simulation of a 300 μm ring.

Figure 3.5: Output spectrum for a simulation of a 30 μm ring.

In the filtered output power graphs (Figures 3.2b and 3.3b) it can be noticed that the steady-state mean power is higher for the shorter ring. This could be counter intuitive as

a larger ring means greater gain due to a larger gain medium, but as mentioned before, it also means that the power is shared between several modes instead of a single one.

There is also a notable difference in the relaxation oscillation frequency between both rings. With a higher circumference, the round-trip time is longer and the modes take more time to build up, resulting in a decrease from around 6.5 GHz in the 30 μm ring to near 3.5 GHz in the 300 μm one.

3.4.   Output power vs. bias current

The first characterization curve obtained is the evolution of the main mode optical power with an increasing bias current. A sweep from 20 mA to 400 mA is made in 20 mA steps. Two different coupling coefficients are used: 0.1 and 0.2. The results are shown in Figures 3.6 and 3.7.
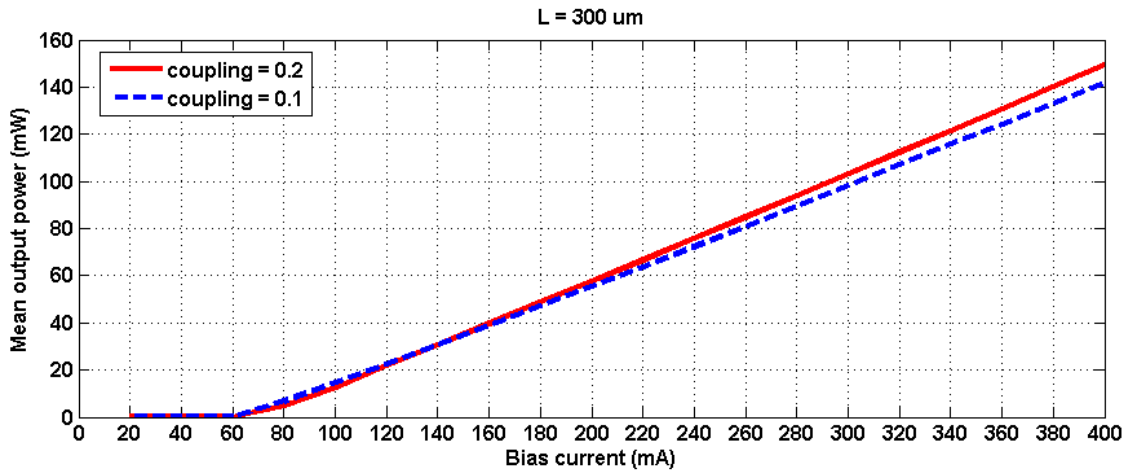
Figure 3.6: Power vs. Current characterization curve for a 300 μm ring laser.
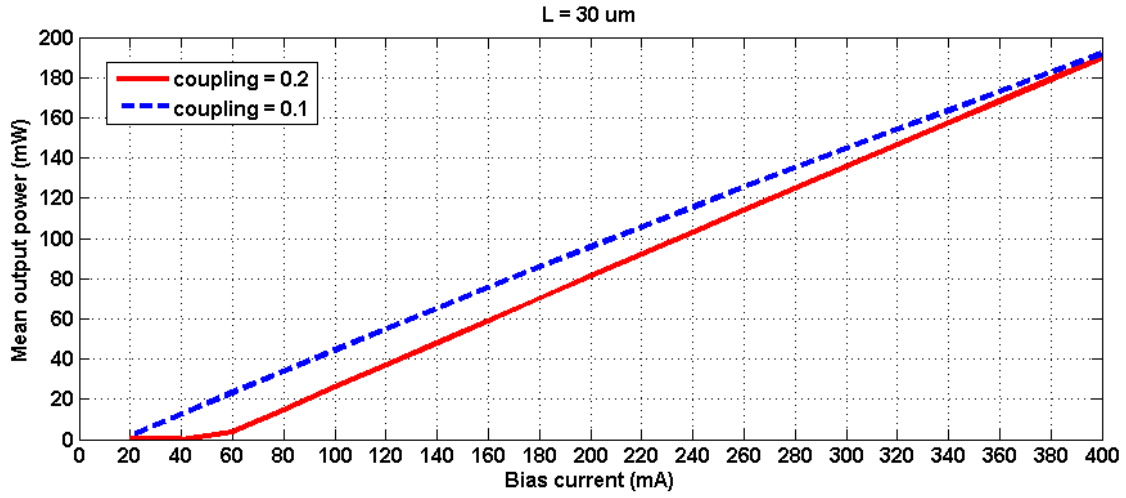
Figure 3.7: Power vs. Current characterization curve for a 30 μm ring laser.

A couple of linear curves appear in both graphs, its slopes being steeper for the 30 μm ring as in that case the main mode gets most of the gain, while it is shared among several modes for the 300 μm ring. The slope is also steeper for the higher coupling value in both cases, as a bigger percentage of the optical power in the ring gets coupled to the waveguide.

By extrapolating the linear curve to the x axis and evaluating the cut point, the threshold current value for lasing can be obtained. The different threshold bias currents for each scenario are shown in table 3.1.

	$α_c = 0.1$	$α_c = 0.2$
L = 300 μm	$I_{th} \approx 60$ mA	$I_{th} \approx 66$ mA
L = 30 μm	$I_{th} \approx 20$ mA	$I_{th} \approx 45$ mA

Table 3.1: Threshold bias current values for different ring lengths and coupling factors

The higher current needed to reach threshold in the longer ring can also be explained by the several allowed modes competing for the same number of carriers. Lower coupling factors also translate into lower threshold current values as a lower percentage of the optical power is coupled to the waveguide, which means a reduced figure for the total losses in the cavity.

An experimental characterization is performed in the laboratory for comparison using the smallest ring available. For the device, the circumference is 2 mm, much longer than the ones studied in this chapter. Therefore, only a qualitative comparison could be done. The results are plotted in Figure 3.8.
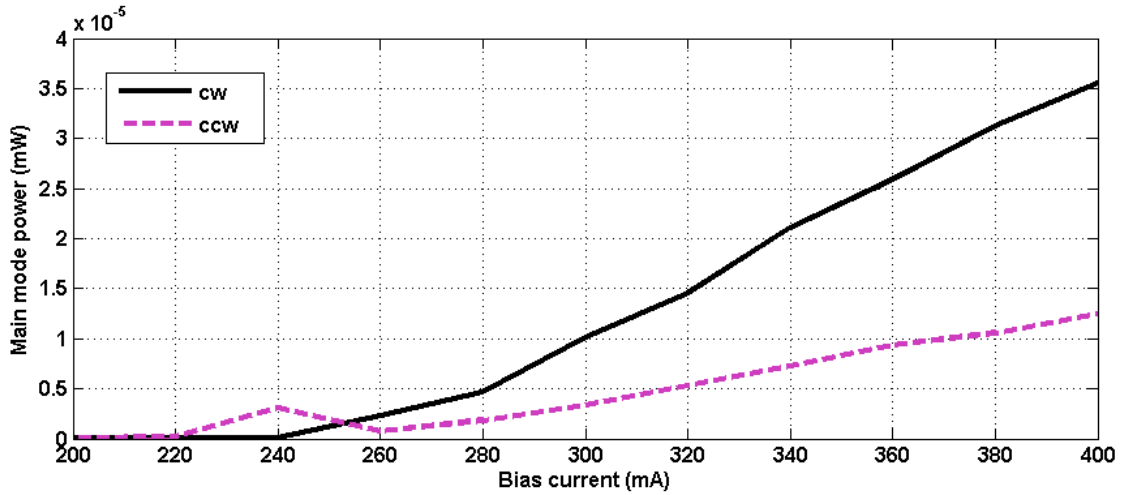

Figure 3.8: Experimental Power vs. Current characterization for a 2 mm ring laser.

Two curves are observed. The power detected is much lower than those the simulation predicts, as there are many losses in the measuring (fiber coupling, connectors, etc.). This is also responsible for the apparently much higher threshold current value, as the power output for current values lower than 220 mA was below the noise level in the optical spectrum analyzer employed for the measures. The curves are linear like in the simulations, but in this case clockwise and counterclockwise outputs have different slopes. This is attributed to asymmetries in the ring and in the coupler sections, which do not exist in the numerical model.

3.5.   Main mode wavelength vs. bias current

From the same set of simulations as in the previous section, the evolution of the main mode wavelength with the bias current is obtained. Only the values for currents above threshold are plotted, the curves are shown in Figures 3.9 and 3.10.
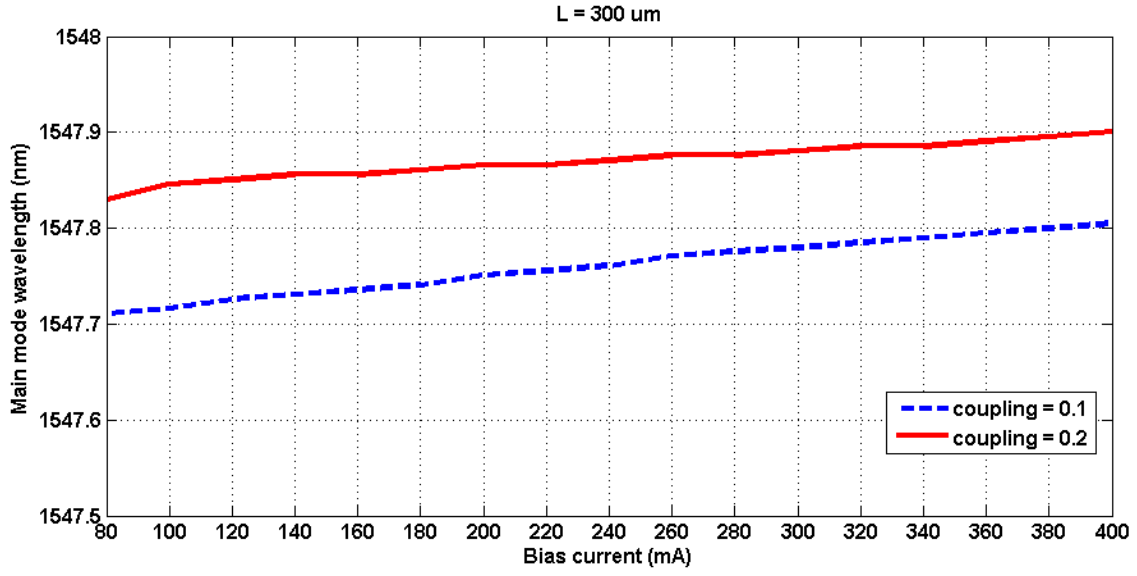
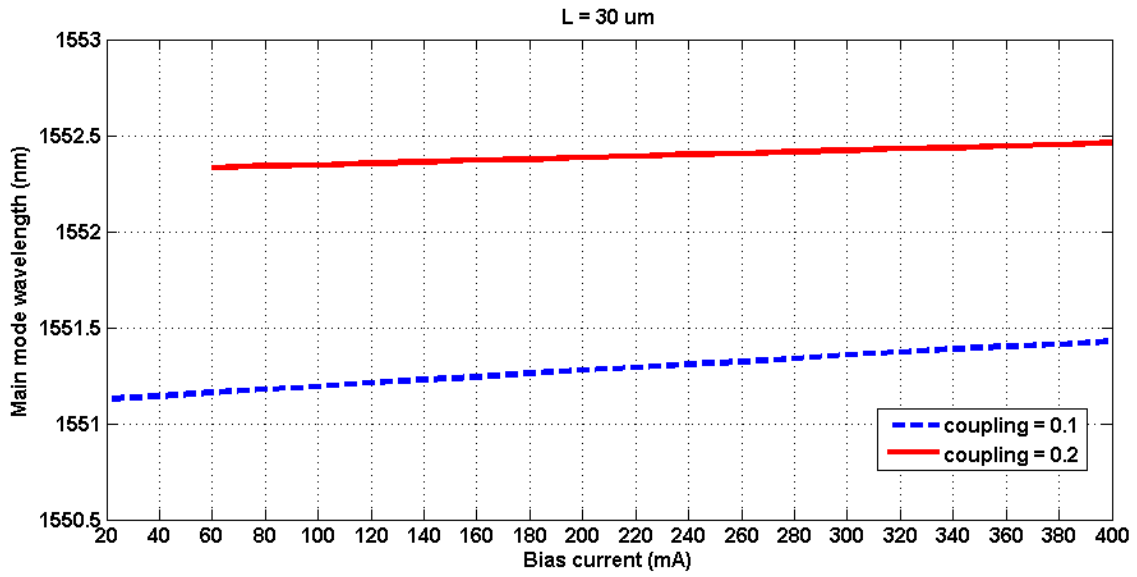*Figure 3.9: Main mode wavelength vs. Current characterization curve for a 300 μm ring laser.*

Figure 3.10: Main mode wavelength vs. Current characterization curv for a 30 μm ring laser.

The curves show how the wavelength linearly increases with the current applied. This is due to the fact that the field phase depends on the gain which is directly linked to the carrier density, and therefore to the injected current. To see this more clearly the field propagation equation in Eq. (2.2.7) can be decomposed in Photon density and phase components:

$$\frac{\partial S_{cw/ccw}}{\partial z} = \left(\Gamma g - \alpha_{\mathrm{int}} - \Gamma_2 \beta_2 S - \Gamma \beta_c n_c - \Gamma \beta_v n_v \right) S_{cw/ccw} \tag{3.5.1}$$

$$\frac{\partial \phi_{cw/ccw}}{\partial z} = \frac{1}{2}\alpha_N \Gamma g - \frac{1}{2}\alpha_2 \Gamma_2 \beta_2 S_t \tag{3.5.2}$$

where S_t in the second term at the right hand is the total photon density.

It can also be seen how with a higher coupling factor the wavelength increases.

The experimental characterization obtained in the laboratory is displayed in Figure 3.11. As in the power vs. current experimental characterization, the results are slightly different for the clockwise and counter clockwise fields, attributed to asymmetries in the ring. The curves also show a linear increase in the wavelength with the current applied, though in some points the higher power output jumps from one mode to the adjacent resonant one. This occurs because its circumference is one order longer than the larger of the simulated rings, and therefore many more modes compete for the carriers: the higher power may jump from one mode to another when the device operating conditions are altered.
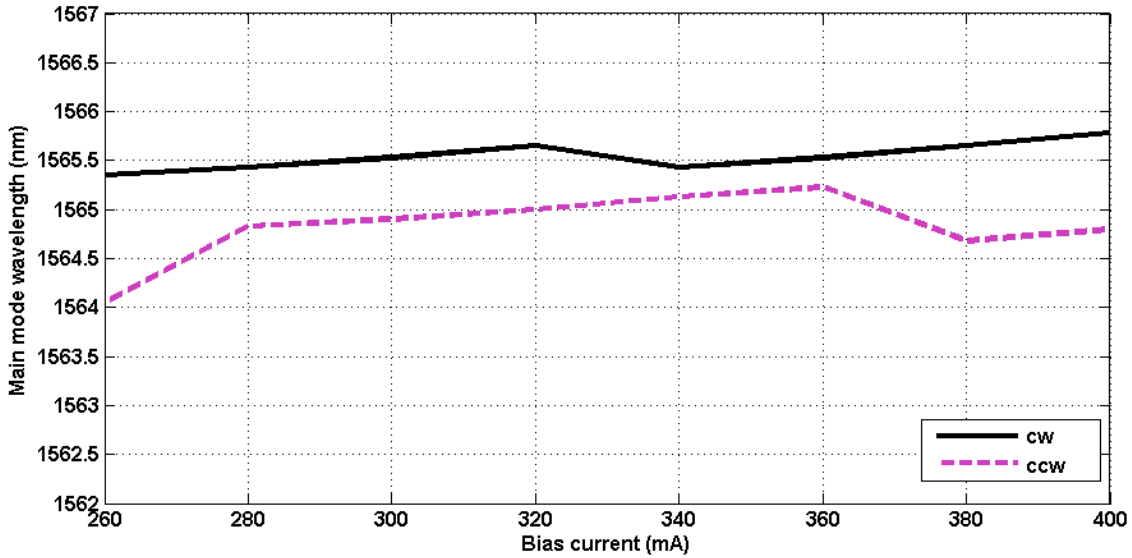

Figure 3.11: Experimental Wavelength vs. Current characterization for a 2 mm ring laser.

Mode jumps can be seen between 320 mA and 340 mA for the clockwise direction and between 360 mA and 380 mA for the counter clockwise direction.
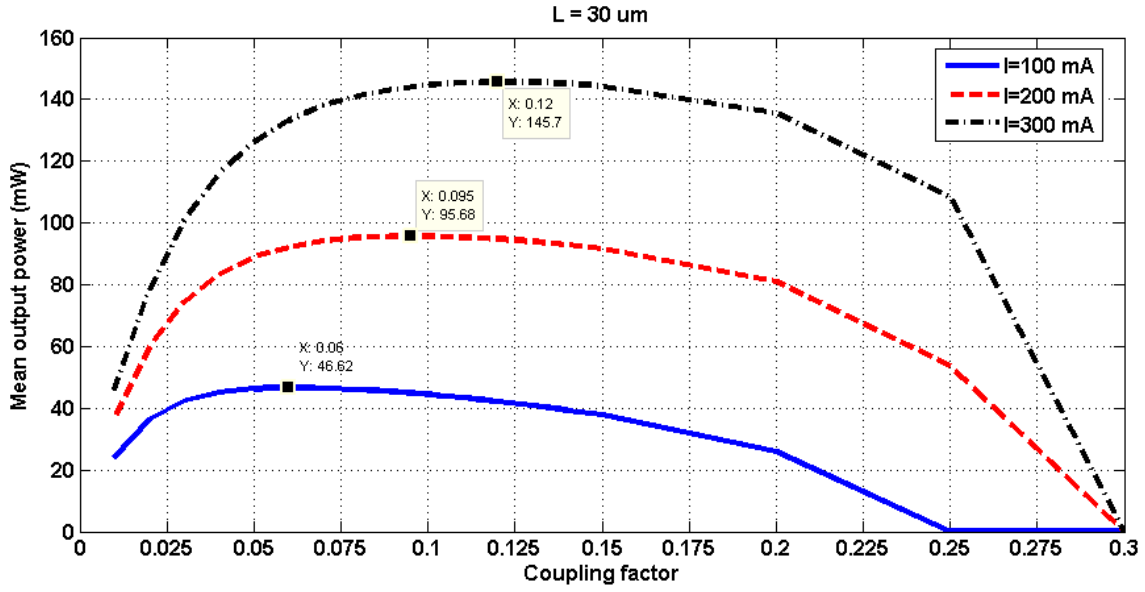
3.6. Output power vs. coupling factor

The coupling factor determines the amount of optical power that is kept in the ring as lasing feedback and the amount that gets coupled to the output waveguide. A lower coupling factor means high optical feedback and thus higher stimulated emission, but also a lower percentage of these photons going to the output. A higher coupling factor means less optical feedback but a higher percentage of the light reaching the output. Therefore, an optimum value for the coupling factor that maximizes the output power is expected for a given set of parameters. In order to evaluate the optimum coupling, a characterization curve of output power vs. coupling factor value has been obtained for three different bias currents. The results are shown in Figures 3.12 and 3.13.

It can be observed how the optimum coupling value increases with the bias current for both short and large rings. It was shown in Figures 3.6 and 3.7 how a higher current translates into higher output power as the gain increases, which is the reason for the curves in Figures 3.12 and 3.13 to increase. The optimum coupling also increases: with a higher gain: less optical power needs to be kept in the loop as feedback and more power can be coupled to the output waveguide, shifting the curves to higher coupling factors.
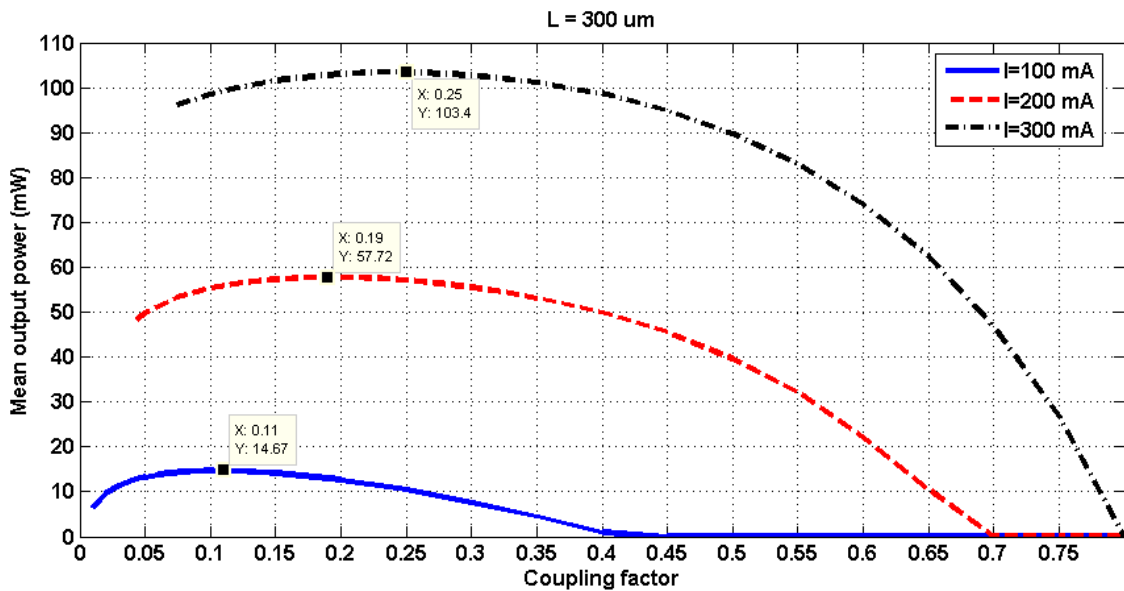
3.12: Power vs.Coupling factor curve for a 300 μm ring.

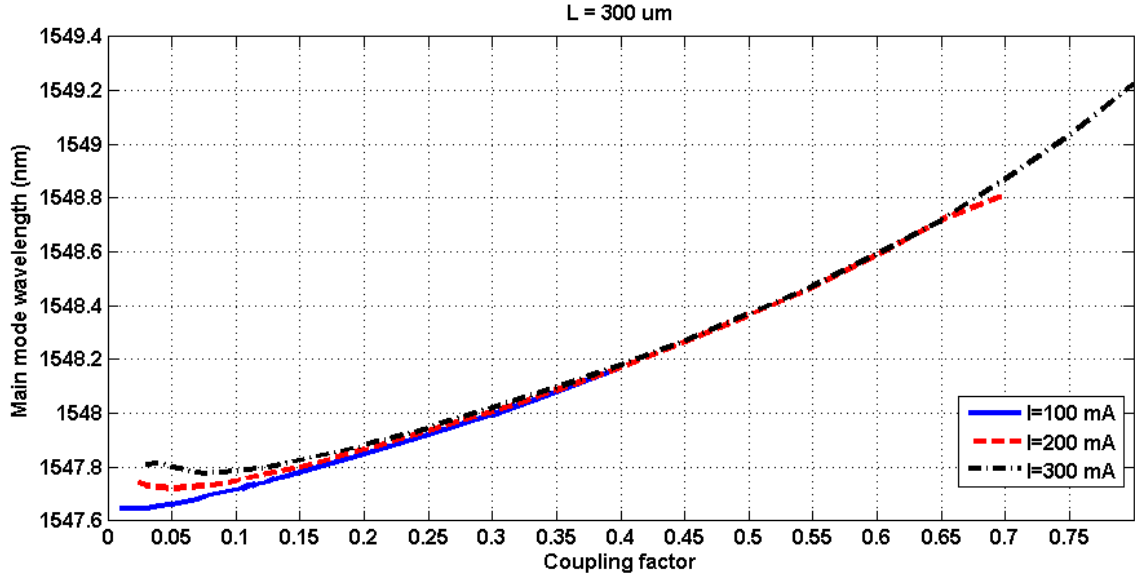*3.13: Power vs.Coupling factor curve for a 30 μm ring.*

In Figure 3.12 the curves are lower than the ones in Figure 3.13, due to gain competition between the modes in the larger ring. However, the optimum coupling is higher, as a larger ring imposes a higher gain.

The optimum coupling factor is situated around α_c=0.2 for a 300 μm ring, and around α_c=0.1 for a 30 μm ring. Notwithstanding, a coupling factor of α_c=0.2 was selected for the 30 μm ring study shown in the next chapter, as it is closer to the actual α_c=0.25 values for the available devices.

3.7.   Main mode wavelength vs. coupling factor

The last characterization curve studied in this chapter is the evolution of the main mode wavelength with the coupling factor; results are displayed in Figures 3.14 and 3.15.

3.14: Wavelength vs.Coupling factor curve for a 300 μm ring.
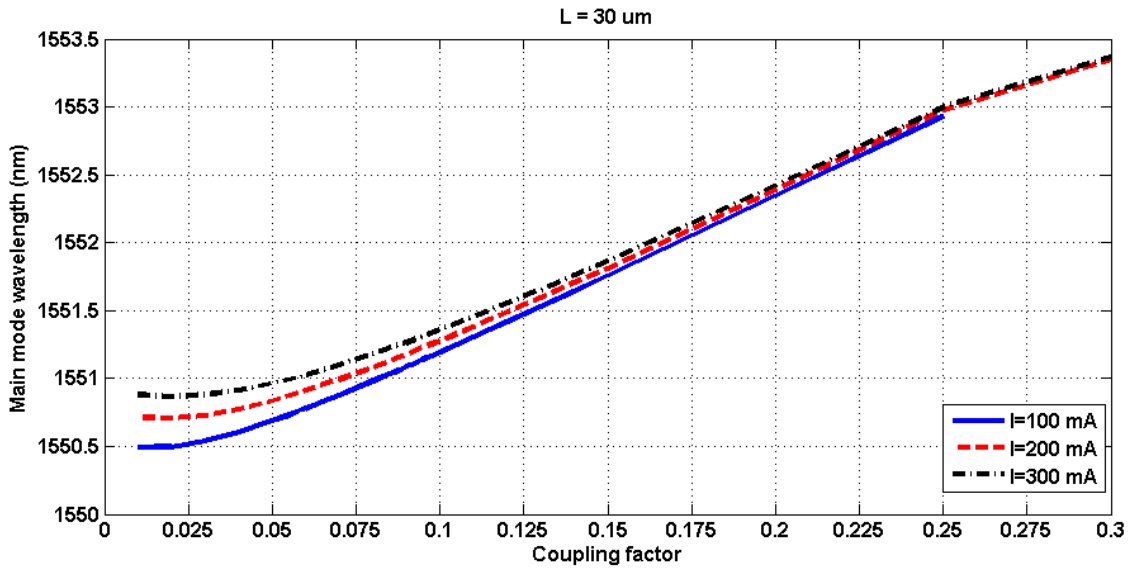
3.15: Wavelength vs.Coupling factor curve for a 30 μm ring.

The curves show the main mode wavelength increasing significantly with the coupling factor. As seen in Eq. 3.2.2 the field phase also depends on the optical power inside the ring, but with opposite sign respect to the gain dependency. Unlike, the output power, the internal optical power decreases monotonously with an increasing coupling factor. Less power also means less carriers being depleted and therefore more available gain in the material. The contribution of these effects take account for the monotonously increasing curves shown above, and for their slope being steeper than the ones shown in

Figures 3.9 and 3.10. This should be taken into account when using ring lasers where the output waveguide is made of active material, as a change in the carrier density can mean a change in the refractive index, and therefore a change in the coupling factor. That way an active coupler may introduce a significant chirp on the signal and a broadening of the lasing modes. This variation seems to be more acute for the smaller ring (Figure 3.11a).

3.8. Bistability

One of the most interesting behaviors of ring lasers that have been observed in experimental research is bistability between clockwise and counter clockwise propagation fields. Under certain bias values, a stable suppression of one of the propagation directions by the external injection of an optical pulse has been observed, [21]. The lasing conditions can also be reversed by injecting a pulse in the opposite direction. This property of ring lasers has already been exploited to achieve an optical flip-flop using two coupled micro-ring lasers [19], and might have many other applications.

This behavior is not observed in the simulations of the model used in this thesis. The reason for this is that the model developed is essentially symmetrical, and for a system to be bistable it needs to have a kind of asymmetry.

The only source of asymmetry in the model at its present state is the spontaneous emission noise, but the random asymmetry it introduces in the system is compensated by the optical coupling between the counter propagating fields that occurs due to reflections at the coupler (which are symmetrical). This can be clearly seen in Figure 3.1; the clockwise and counter clockwise fields show different evolutions in the beginning due to the random nature of the noise that is building them up, but they quickly achieve the same steady-state due to the coupling between the modes by the reflections.

The physical reason for the bistability in real devices is not clear, but it might be caused by irregularities in the ring waveguide or/and in the coupler that would provoke asymmetrical reflections, and therefore an asymmetrical coupling between the counter-propagating fields. Some models reported in the literature so far, also introduce an

asymmetric gain compression factor. However, experimental results do not show a strong proof for it.

Chapter 4

Wavelength conversion in a 30 µm micro-ring laser

4.1. Introduction

After the characterization of the micro-ring laser model, numerical experiments related to ultra-fast dynamics for high-speed signal processing in semiconductor materials, are carried out.

To do so, a particular scenario is considered: the use of a microring laser for all-optical wavelength conversion. This can be achieved by the external injection of optical pulses tuned at one of the first resonant frequencies. This way, a saturation of the material gain is expected via depletion of the carriers, effectively suppressing all modes (or even shutting down the laser) for a brief period of time. Therefore, the laser will work as a wavelength converter with inversion, as for each pulse received at the first resonant frequency, a drop in the power of the main mode will occur.

In this chapter the dynamic response of a 30 µm ring laser under injection of isolated pulses is studied, and following, the response to different bit-rate signals is tested. Short Gaussian pulses in the pico-second scale have been chosen for the experiments, to show the performance of the laser in this interesting operation regime. Anyhow, other different signals such as rectangular pulses can be used by modifying the input parameters of the simulator.

4.2. Measuring relaxation oscillation frequency and rise-time

The concept of the relaxation oscillation was introduced and explained in the previous chapters. This oscillation has a relatively high time-scale (hundreds of picoseconds) compared to the pico-second and sub-picosecond time-scales of the intra-band carrier-photon and carrier-carrier interaction times.

It is therefore expected that the relaxation oscillation will play a strong role to determine the recovery time after the external injection of the pulses. The influence of the bias current and the injected pulse energy upon the relaxation oscillation and signal rise-time is studied in this section.

To carry out this study, a single Gaussian pulse tuned to the first resonant mode is injected in the clockwise waveguide port. The spectrums of the input and output signals upon injection of a 2 ps width and 1 W peak-power pulse are displayed in Figure 4.1.
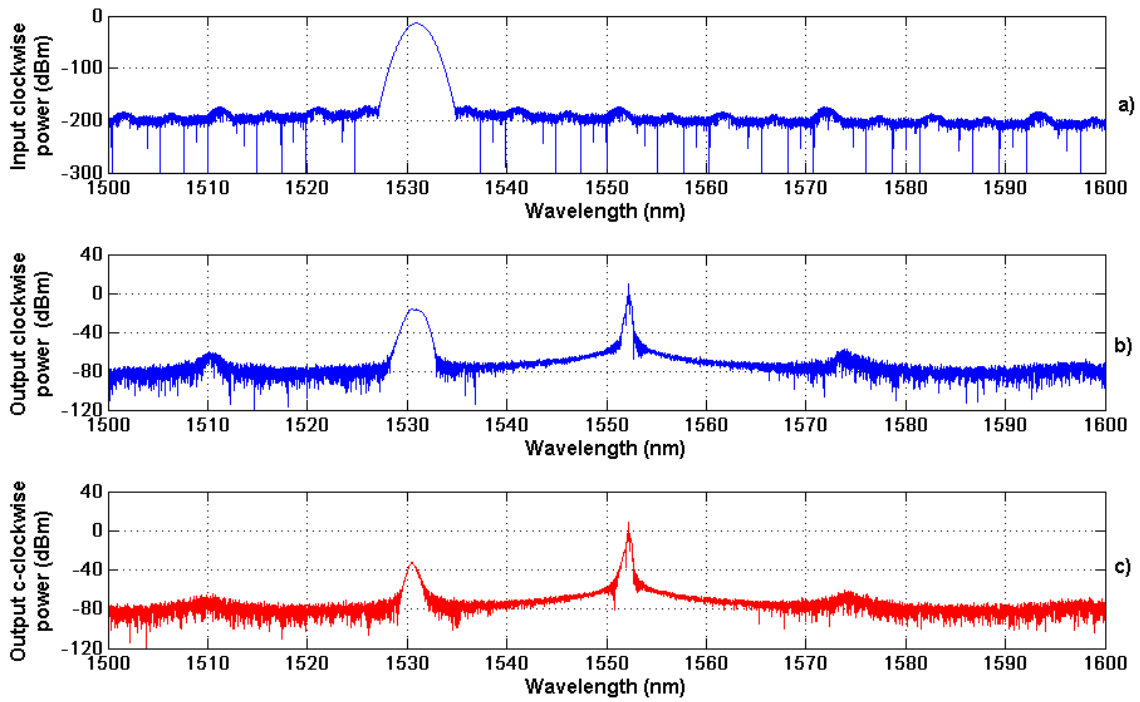
Figure 4.1: Optical power spectrums upon injection of a Gaussian pulse. a) Clockwise input signal. b) Clockwise output signal. c) Counter clockwise output signal.

It can be seen how the pulse appears in the clockwise output spectrum. There is also some coupling to the counter clockwise direction due to the reflections in the coupler.

4.2.1.   Effect of the bias current on the relaxation oscillation

To evaluate the response of the micro-ring laser under ultra-fast excitations, both the relaxation oscillation and the recovery time were evaluated. The relaxation oscillation was measured using the first two maximums of the oscillation. The rise time is defined as the time the power takes to rise from 20% to 80% of the difference between the

power level while being suppressed and the level at the first maximum of the relaxation oscillation right after the incoming pulse.

These properties are measured for the initial start-up oscillation, that is, from zero to the operating current under no optical injection, and for the dynamic response to a Gaussian pulse 2 ps in width and 400 mW of peak power. The simulations are repeated sweeping the bias current from the threshold value to 400 mA in steps of 20 mA.

For a clear visualization of the experiment, an example of the input and output signals for $I = 100$ mA and $I = 300$ mA simulations is shown in Figure 4.2.
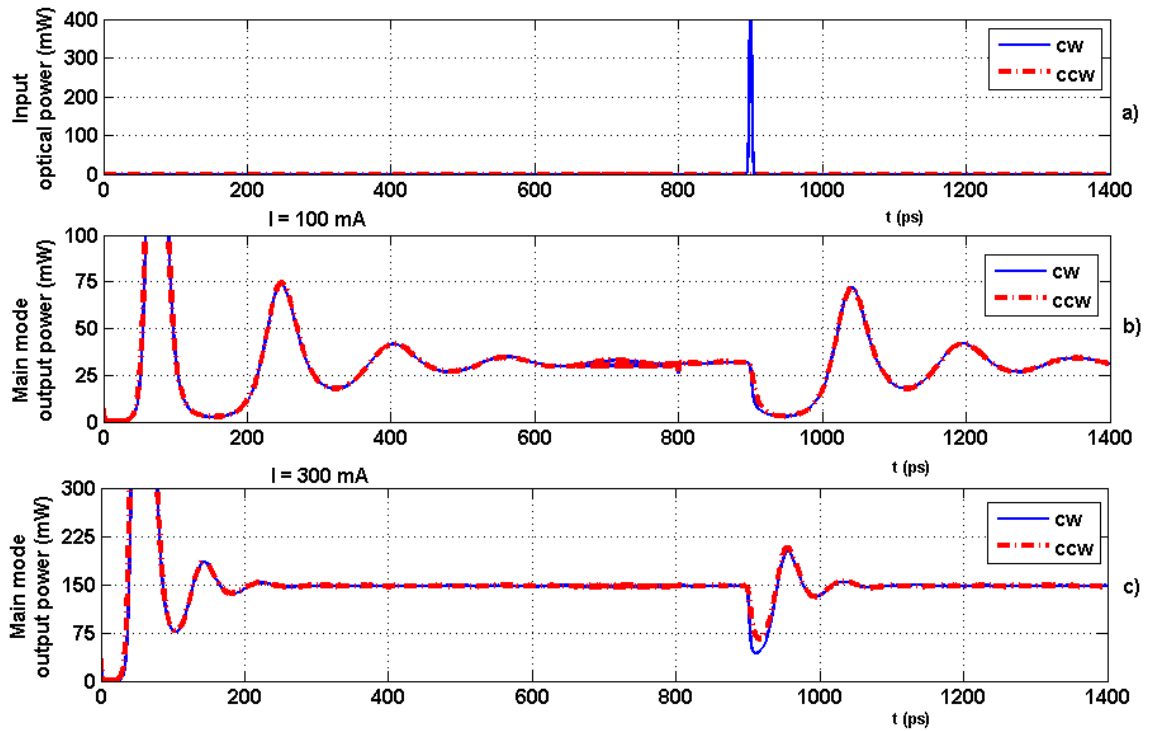

Figure 4.2: Optical power signals for the study of relaxation oscillation. a) Input signals (equal for both cases). b) Output signal for I=100 mA. c) output signal for I=300 mA.

It can be clearly seen how the suppression of the main mode remains long after the pulse has ended. Even when the pulse is as short as 2 ps the relaxation oscillation makes the laser take much longer than that to recover back to the steady-state even for such a short laser. In Figure 4.2b it is observed how the initial and dynamic relaxation oscillations have apparently the same frequency. Comparing with Figure 4.2c it can be expected that the higher the current, the higher the relaxation oscillation frequency will be. A curve showing the evolution of the initial and dynamic relaxation oscillation frequencies with the bias current obtained from the sweep is shown in Figure 4.3.
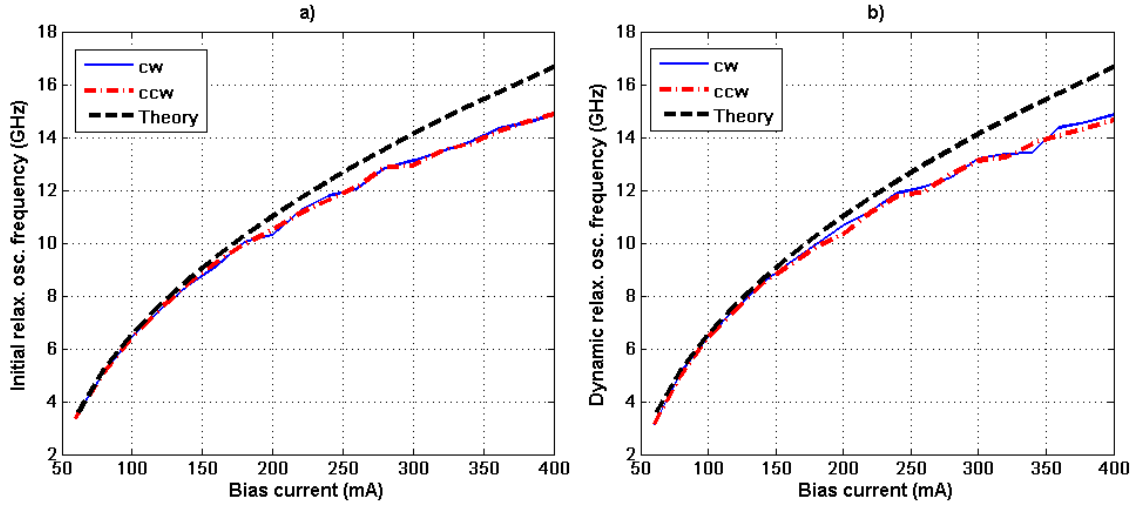
Figure 4.3: Optical Relaxation oscillation frequency vs. bias current. a) At initial build-up.
b) After external pulse injection.

The curve indeed shows the frequency increasing with the bias current, this indicates that to achieve a faster response high bias should be used. The curves have almost equal values for clockwise and counter clockwise directions, as in the model both are coupled via the back reflections in the coupler. However, the curves are also almost identical for the initial and dynamic oscillations, which leads to think that the properties of the pulse will have little influence on the response time. This will be further studied in the next section.

Plotted in dotted line is a theoretical approximation of the relaxation oscillation frequency f_R using the formula [24]:

$$f_R = \frac{1}{2\pi} \sqrt{\frac{a}{qV}\left(I - I_{th}\right) - \frac{1}{t_n t_p}} \tag{4.2.1}$$

where t_n is the carrier lifetime and t_p is the photon lifetime, which follows the expression:

$$t_p = \frac{1}{v_g \left(\alpha_{int} - \alpha_f\right)} \tag{4.2.2}$$

Here α_{int} refers to the internal losses and α_f to the losses in the feedback, that is, losses in the coupler for our model. They can be calculated as:

$$\alpha_f = \frac{1}{L} \ln\left(\frac{1}{\alpha_c}\right) \tag{4.2.3}$$

where L is the circumference of the ring and α_c is the coupling factor.

The value for the threshold current used is I_{th} = 45 mA obtained through characterization in the previous chapter (Figure 3.7b). The simulated and theoretical curves are a close match, the slight difference probably being due to small inaccuracies in the method employed to calculate the relaxation oscillation frequency, or the threshold current from the data and the fact that in the approximation given by Eq. 4.2.1, the effects of TPA and FCA are not taken into account.

The evolution of the rise-time is also plotted against different bias current values. The results are shown in Figure 4.4.
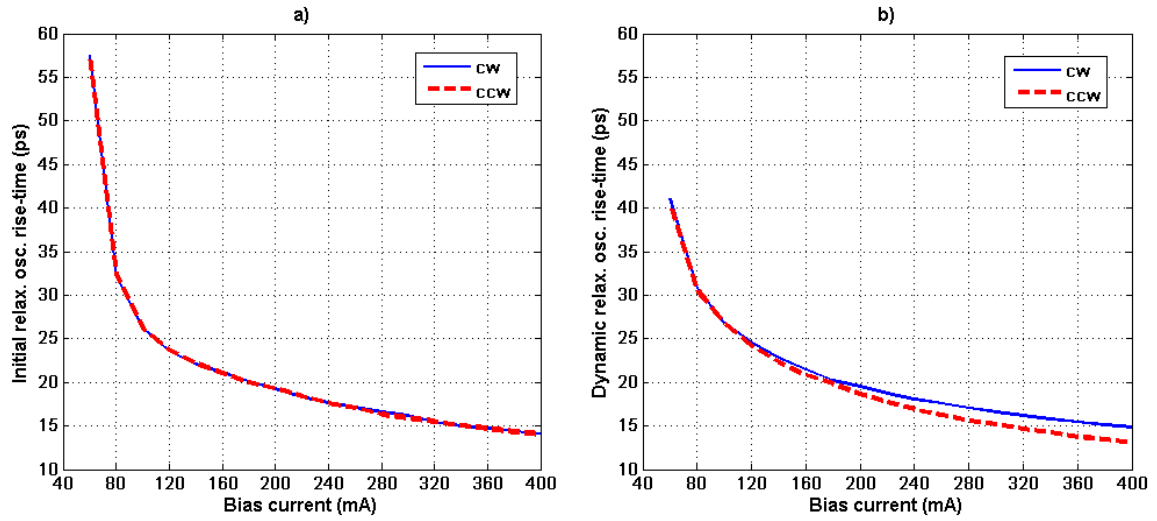

Figure 4.4: output power rise-time vs. bias current. a) At initial build-up.
b) After external pulse injection.

The curves show how the rise-time decreases with a higher current, in concordance with the evolution of the relaxation oscillation. However, even for current values as high as 400 mA, the rise-time is only reduced to 15 ps. This means that 40 Gb/s transmissions are unlikely to succeed in this scenario, as the pulses would repeat each 25 ps, very close to the rise-time for very high bias, and equal or smaller than the rise-time for lower currents. The mismatch between clockwise and counter clockwise values in Figure 4.4b is because the clockwise field gets slightly more suppressed as the pulse is injected in that direction.

As commented above, increasing the bias current, the relaxation oscillation can be increased, and therefore the rise time reduced. However, as shown by the graph, the relaxation oscillation shows a square root behavior with the bias current, in agreement with the theory. This implies, that to reduce the rise time to a half, the bias current must be increased about four times. Therefore, it is expected that fast operation of such devices would require high electrical pumping currents, with may arise as a critical drawback.

4.2.2. Effect of the pulse energy on the relaxation oscillation

The next step is to check if the device response can be improved by varying the energy of the injected signal. To do this the dynamic relaxation oscillation and rise-time are measured for different energy pulses. On a first set of simulations the energy of the pulses is changed by varying the peak power from 200mW to 10W, with a fixed width of 2ps. The results are displayed in Figures 4.5 and 4.6. A table matching Gaussian pulses peak power with their energies for a width of 2ps is shown in Table 4.1.
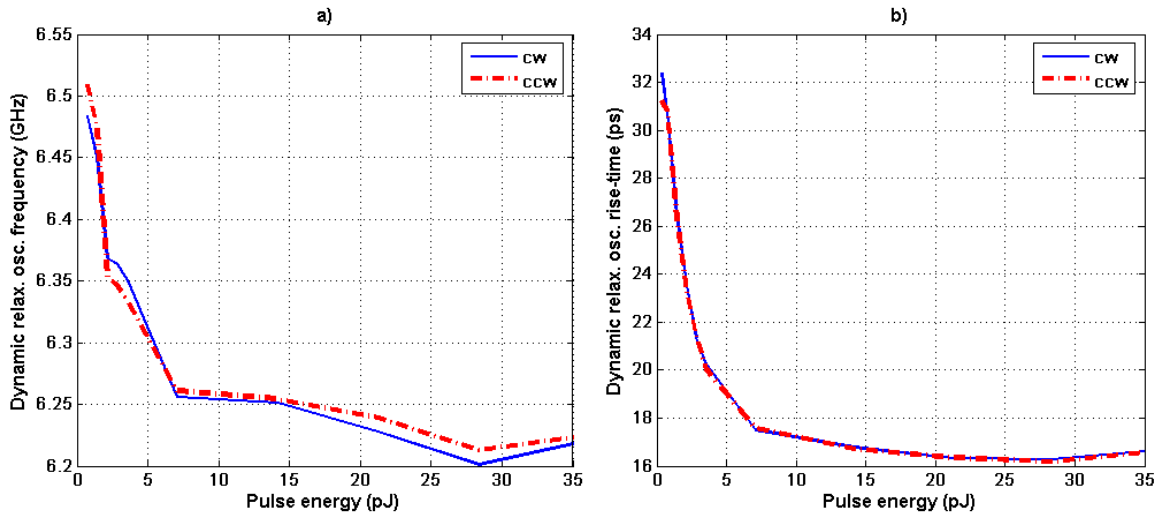

Figure 4.5: Dynamic response study varying pulse peak power. a) Measured relaxation oscillation frequency. b) Measured rise-time.
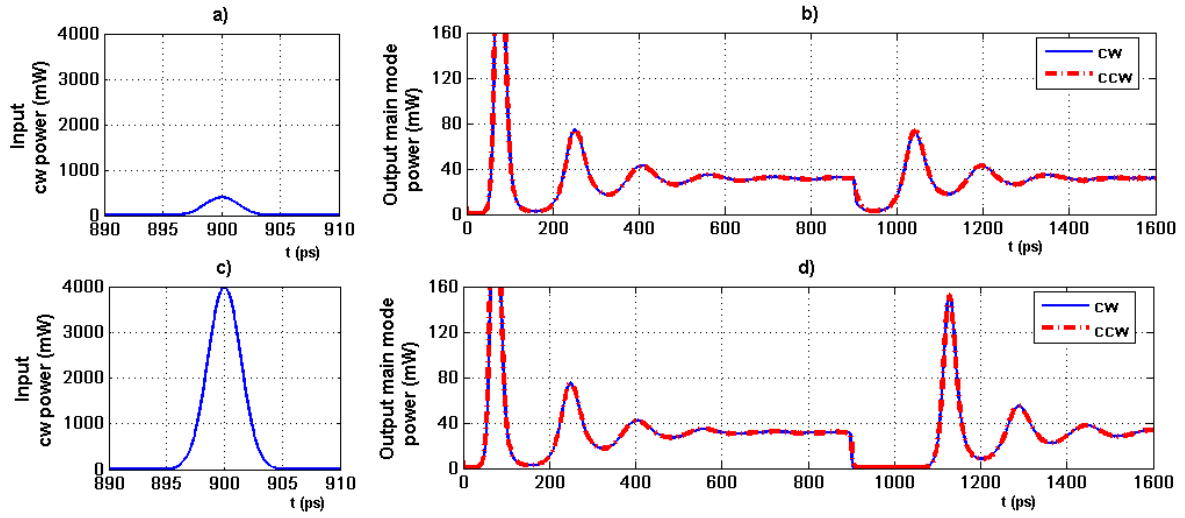
Figure 4.6: Time domain examples of the dynamic response to external injection.

a) and b): input and output powers in the case of a 400mW and 2 ps pulse.

c) and d): input and output powesr in the case of a 4W and 2 ps pulse

Pulse peak power	Pulse energy
100 mW	0.35 pJ
200 mW	0.71 pJ
400 mW	1.42 pJ
600 mW	2.13 pJ
800 mW	2.84 pJ
1 W	3.54 pJ
2 W	7.09 pJ
4 W	14.18 pJ
6 W	21.27 pJ
8 W	28.36 pJ
10 W	35.45 pJ

Table 4.1: Gaussian pulse energies for different peak powers at a width of 2ps.

It can be seen in how the effect on the measured relaxation oscillation frequency and rise-time is much weaker than when varying the bias current. There is also an apparent discrepancy: while the measured relaxation oscillation frequency decreases, so does the rise-time. This is caused by the behavior of the first overshoot of the relaxation oscillation. The higher the pulse energy is, the more suppressed the main mode will be and the higher and steeper the first overshoot will rise, accounting for the decrease in the rise-time. However, if the first overshoot is high enough it could saturate the gain so much as to cause a second suppression, delaying the next maximum (as the relaxation

oscillation frequency is measured by the time separation between maximums, this would explain why it also decreases). To illustrate this, two of the simulations run to obtain the curve are showed in the time domain in Figure 4.6.

On top of the effects on the overshoot, it can be noticed in the figure above that if the pulse energy is too high, the laser is turned off completely, and the time it takes to build back the modes is substantial, in the same order as one period of the relaxation oscillation.

A second set of simulations is performed, where the energy of the pulse is now varied by setting the peak power to 1W and changing the pulse width from 0.2ps to 10ps. The curved obtained and two time-domain examples are shown in figures 4.7 and 4.8. A table matching Gaussian pulses widths with their energies for a peak power of 1W is shown in Table 4.2.
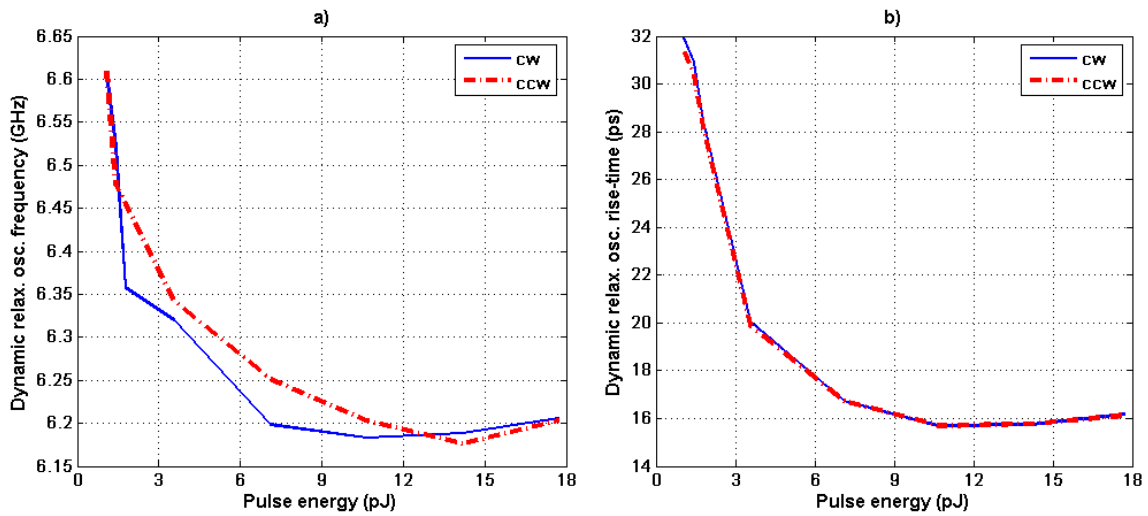

Figure 4.7: Dynamic response study varying pulse width. a) Measured relaxation oscillation frequency. b) Measured rise-time.

The results are similar to those obtained in Figures 4.5 and 4.6, with decreasing curves for both the measured rise-time and measured relaxation oscillation frequency due to the power overshoot and the gain saturation it causes.
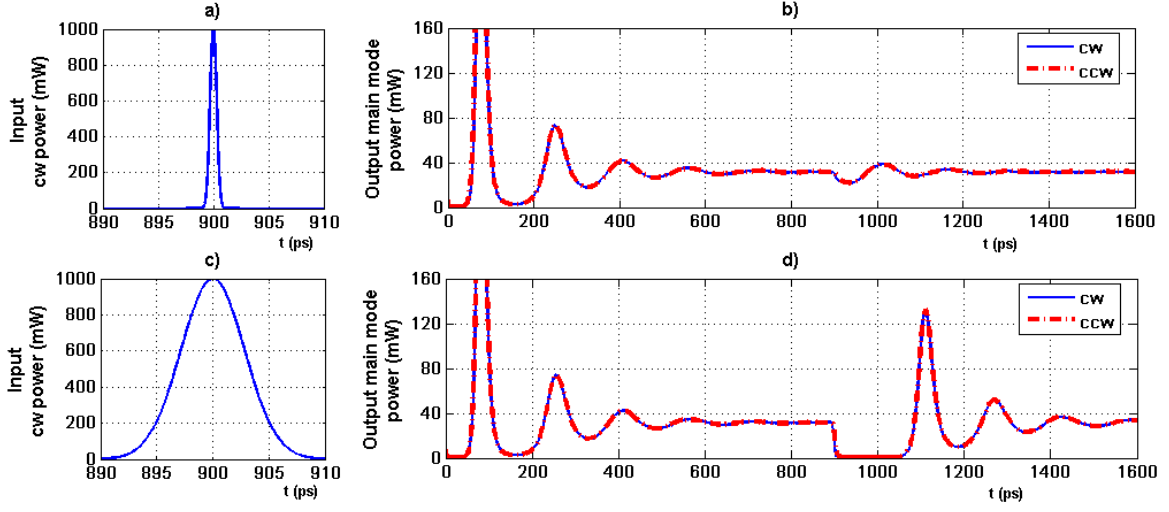
Figure 4.8: Time domain examples of the dynamic response to external injection.

a) and b): input and output powers in the case of a 1W and 0.4 ps pulse.

c) and d): input and output powers in the case of a 1W and 4 ps pulse.

Pulse width	Pulse energy
0.4 ps	0.71 pJ
0.6 ps	1.06 pJ
0.8 ps	1.42 pJ
1 ps	1.77 pJ
2 ps	3.54 pJ
4 ps	7.09 pJ
6 ps	10.63 pJ
8 ps	14.18 pJ
10 ps	17.72 pJ

Table 4.2: Gaussian pulse energies for different widths at a peak power of 1W.

Therefore, the external pulse energy must be chosen carefully: it must be high enough to sufficiently suppress the main mode (and achieve a greater eye opening, as will be shown in the next section), but not as high as to completely shut down the laser or cause a high overshoot, what would delay the recovery of the mode. Notwithstanding, even with an optimized pulse energy, the response time is still mainly determined by the relaxation oscillation, and the viability of reducing it via the bias current may be limited.

4.3. Measuring the eye opening for different bit-rate signals

To finish the research carried out in this thesis, the performance of the micro-ring laser as a wavelength converter under different bit-rate signals is studied.

The particular signal employed consists of a succession of short Gaussian pico-second pulses at a certain rate, their presence meaning a "1" and there absence a "0". However other intensity modulation formats such as NRZ rectangular pulses can be employed.

4.3.1. Performance at 2.5 Gb/s

The eye openings are obtained and analyzed for increasing bias currents and pulse energies, similarly to the previous section. A time-domain trace and eye diagram are plotted to facilitate the analysis of the results in each case. The eye opening is defined as the ratio between the minimum value of the optical power when the incoming bit is a logical "0" and the maximum value of the optical power when the incoming bit is a "1" (notice that the ring is operating as an inverted wavelength converter, so a "0" translates into a high power and a "1" into a low power). This ratio was evaluated for any instant in a bit period, and the maximum value in the optimum decision instant was measured.

The evolution of the eye opening for an increasing bias current is shown in Figure 4.9 and the time domain traces and eye diagrams in Figures 4.10 and 4.11. The pulses used have a 400mW peak power and 2ps in width.
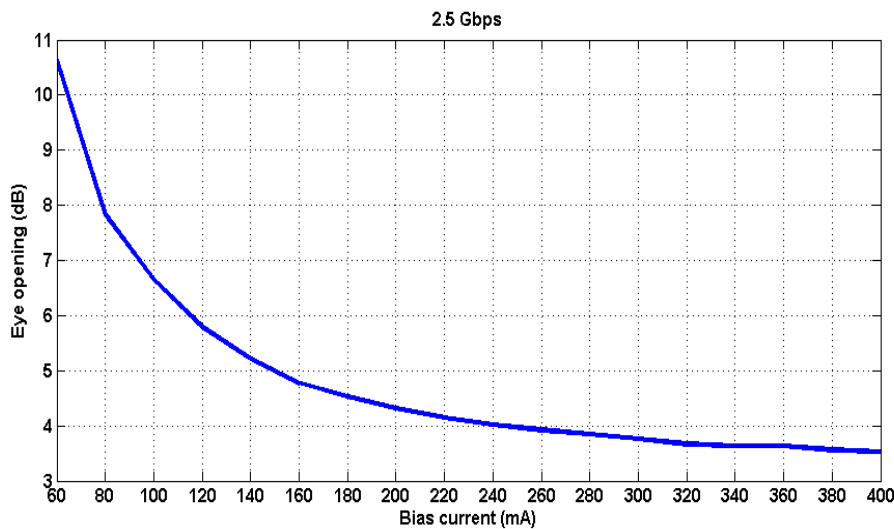

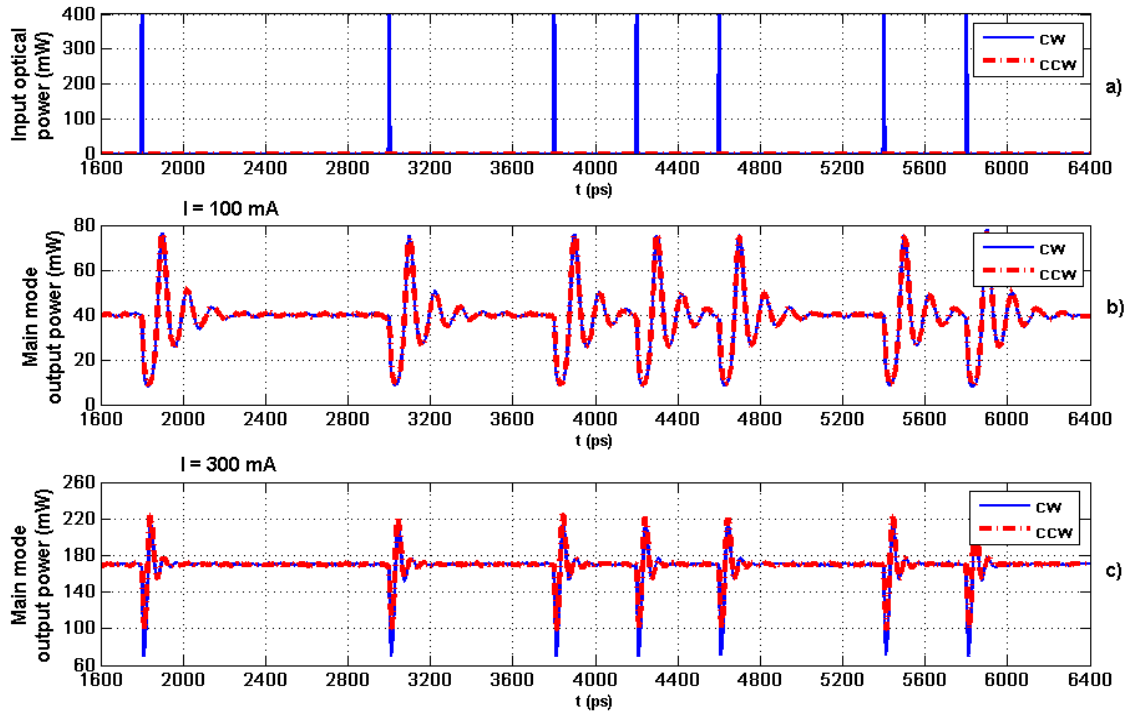*Figure 4.9: Eye opening vs bias current for a 2.5 Gb/s signal.*

Figure 4.10: Time domain examples of the dynamic response to an external 2.5 Gb/s signal.

a) Input signals (equal for both cases). b) Output signal for I=100 mA.
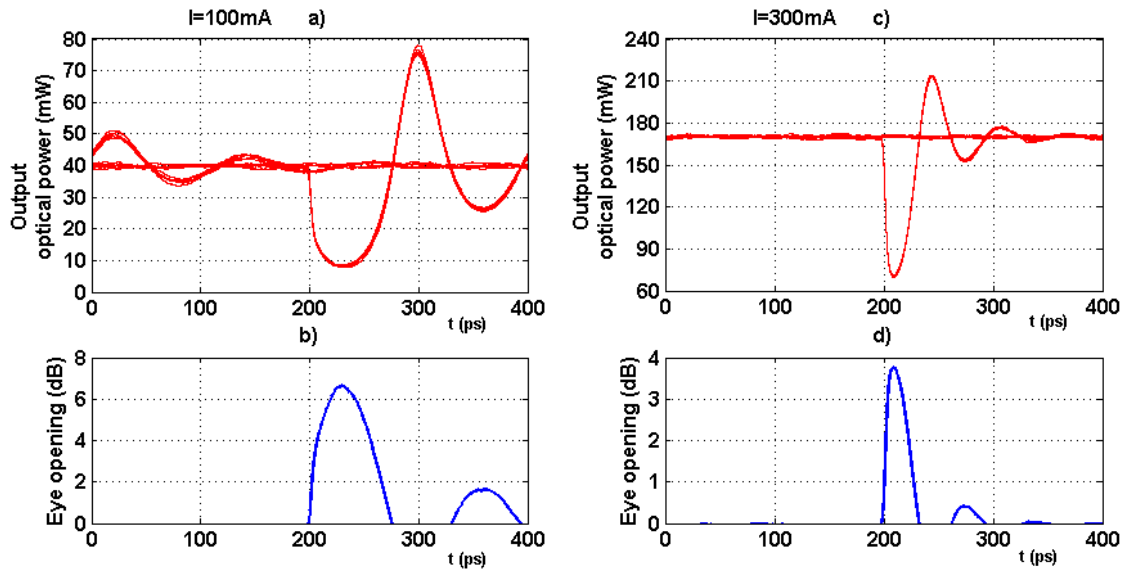
c) Output signal for I=300 mA.

Figure 4.11: Eye diagram examples of the dynamic response to an external 2.5 Gb/s signal.

a) and b): Eye diagram and eye opening curve for I=100mA.

c) and d): Eye diagram and eye opening curve for I=300mA .

Figure 4.9 shows a decreasing eye opening against bias current. In a first glance, it might have been expected otherwise, as with a higher current the relaxation oscillation is faster and therefore so is the recovery time. However, but looking at figures 4.10 and 4.11 it is seen how the saturation caused by an external pulse of fixed energy is weaker for a higher bias than for a lower one. Therefore the extinction-ratio is lower for higher currents and so the eye-opening is also lower. It is also clear how at a bit-rate of 2.5 Gb/s the limited relaxation oscillation frequency is not a problem at any bias current value.

Same as before, the performance with different pulse energies is also tested, the evolution of the eye opening is shown in Figure 4.12 and the time domain traces and eye diagrams in Figures 4.13 and 4.14. The bias has been fixed to 100 mA.
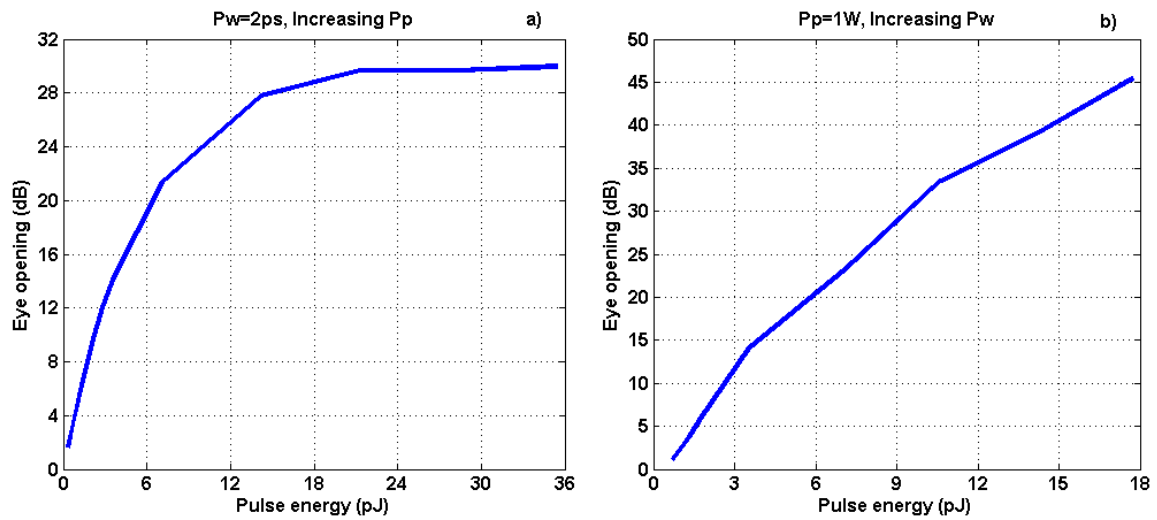

Figure 4.12: Eye opening vs pulse energy for a 2.5 Gb/s signal. a) pulses with a 2ps width and increasing peak power. b) pulses with a 1W peak value and increasing width

Figure 4.12 shows an increasing eye opening against the pulse energy, and in Figures 4.13 and 4.14 it can be appreciated how this is because the more energy the pulse carries, the higher the saturation. For energies higher than 21 pJ the laser is shut-off completely and the eye opening stays constant, it must be stressed that increasing the pulses energy beyond this point increases the device recovery time, which is not critical at 2.5 Gb/s but might be for higher bit-rates.
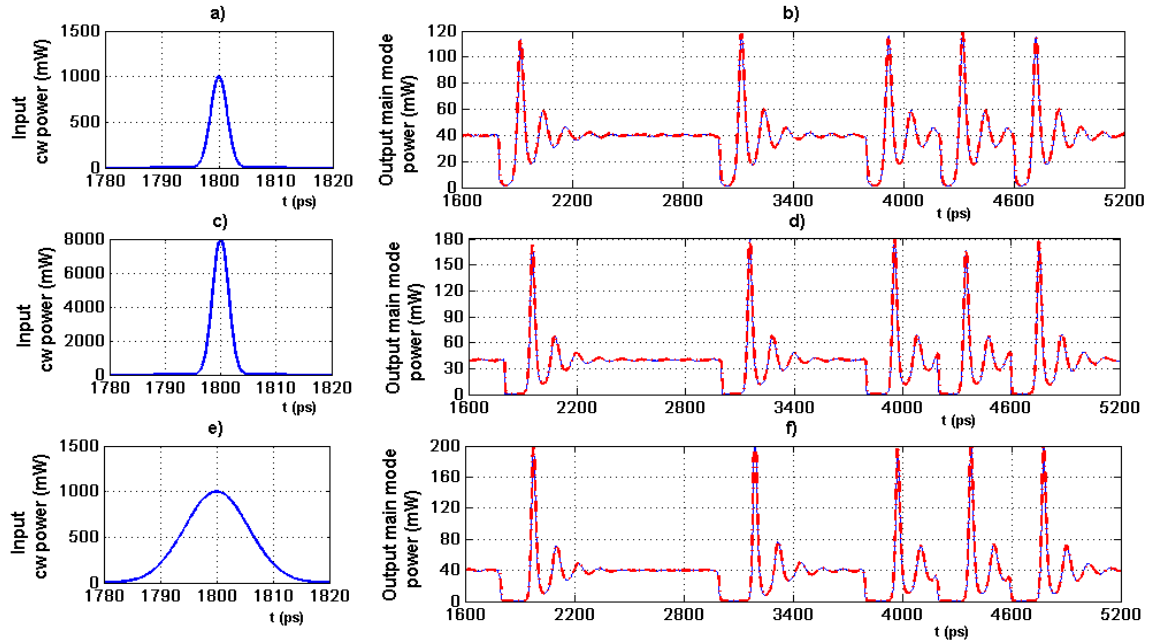
Figure 4.13: Time domain examples of the dynamic response to an external 2.5 Gb/s signal.

a) and b): input pulse example and output power in the case of 1W and 2 ps pulses

c) and d): input pulse example and output power in the case of 8W and 2 ps pulses.

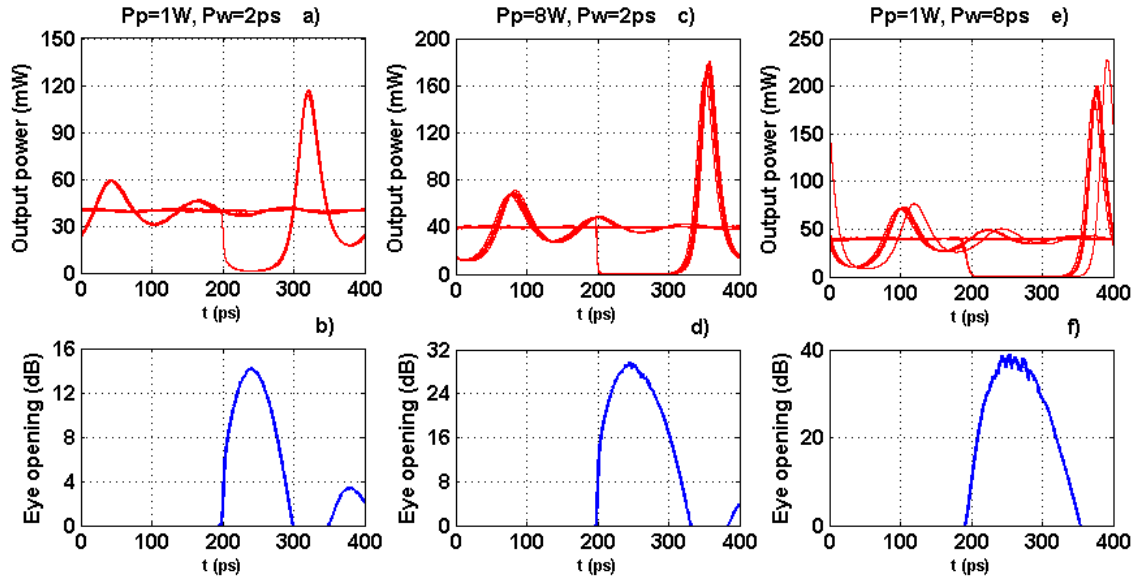*e) and f): input pulse example and output power in the case of 1W and 8 ps pulses.*

Figure 4.14: Eye diagram examples of the dynamic response to an external 2.5 Gb/s signal.

a) and b): Eye diagram and eye opening curve for 1W and 2 ps pulses.

c) and d): Eye diagram and eye opening curve for 8W and 2 ps pulses.

e) and f): Eye diagram and eye opening curve for 1W and 8 ps pulses.

4.3.2. Performance at 10 Gb/s

Once the ability of the micro-ring laser to operate as an all-optical wavelength converter at 2.5 Gb/s with acceptable performance figures has been evaluated, higher bit-rates in which the relaxation oscillation frequency might be an obstacle will be tested.

Once again, eye openings are obtained and analyzed for increasing bias currents and pulse energies, as in the previous subsection.
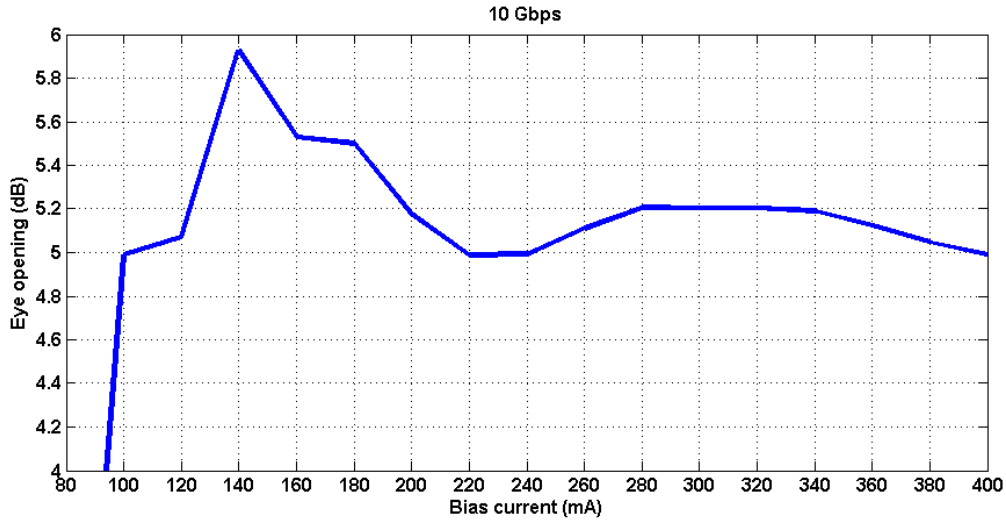

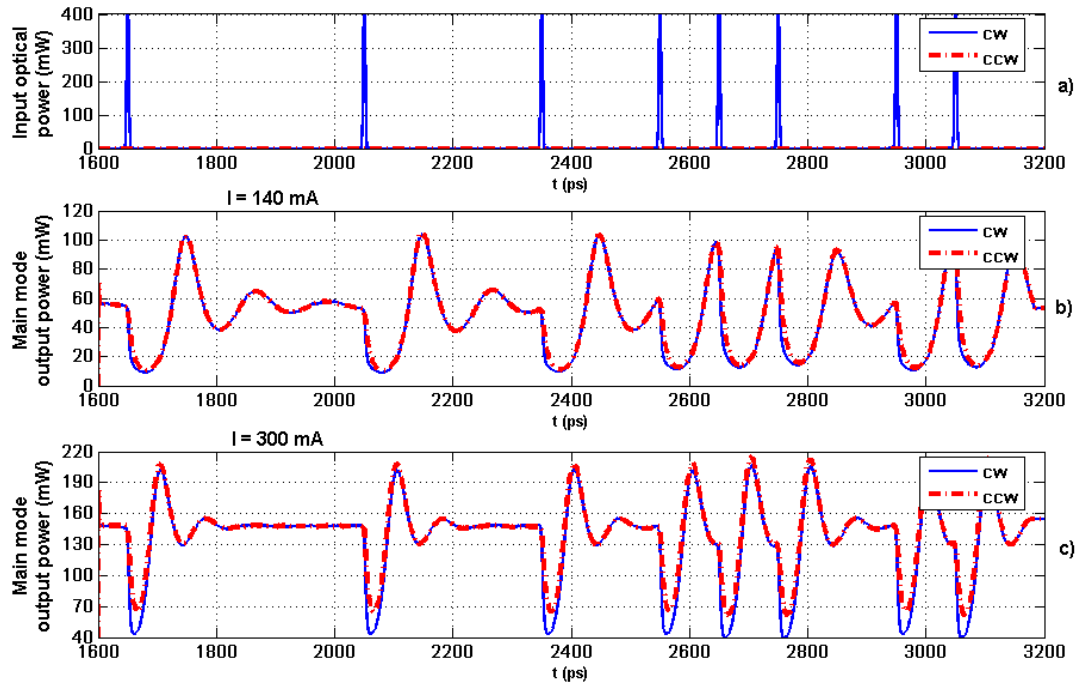*Figure 4.15. Eye opening vs bias current for a 10 Gb/s signal.*

Figure 4.16: Time domain examples of the dynamic response to an external 10 Gb/s signal.

a) Input signals (equal for both cases). b) Output signal for I=140 mA.
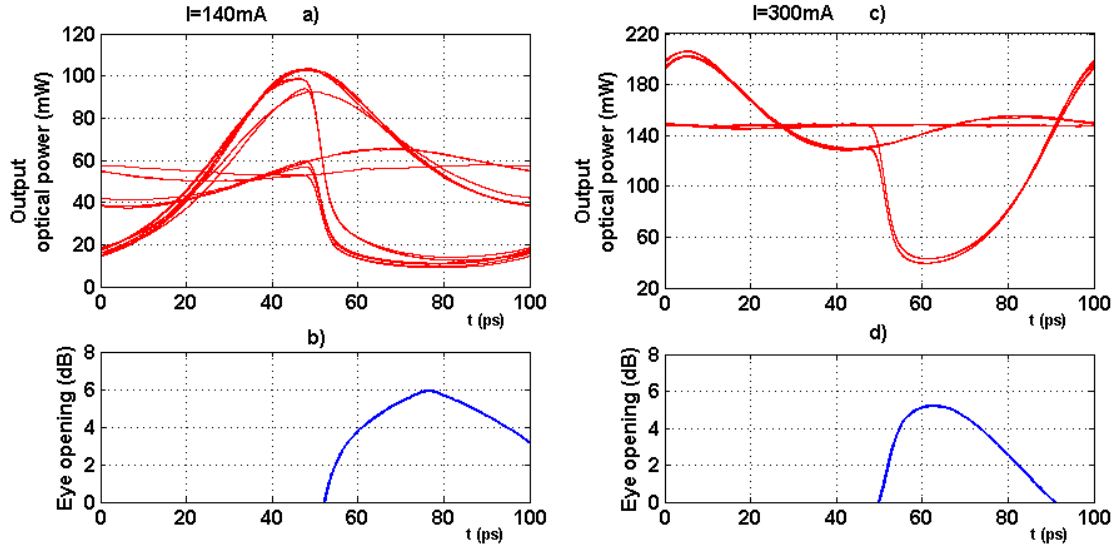
c) Output signal for I=300 mA.

Figure 4.17: Eye diagram examples of the dynamic response to an external 10 Gb/s signal.
a) and b): Eye diagram and eye opening curve for I=140mA.
c) and d): Eye diagram and eye opening curve for I=300mA.

The evolution of the eye opening for an increasing bias current is shown in Figure 4.15 and the time domain traces and eye diagrams in Figures 4.16 and 4.17. The pulses used have a 400mW peak power and 2ps in width.

It is clear from Figure 4.16 how the relaxation oscillation frequency becomes now a critical problem: the laser has not yet achieved the steady state when the next pulse arrives, and the eye opening performance is now also a matter of timing. If the relaxation oscillation frequency is such that the maximums coincide with the pulse time-slots, the eye opening will be greater, as occurs in Figure 4.16b and its corresponding eye diagram in Figure 4.17a. If they do not coincide they eye diagram will be lower, as seen in Figures 4.16c and 4.17c.

This explains the unexpected curve seen in Figure 4.15, with an optimum followed by a decreasing value, corresponding to the pulse time-slots matching relaxation oscillation maximums and minimums, respectively.

Next, performance with different pulse energies is tested, the evolution of the eye opening is shown in Figure 4.18 and the time domain traces and eye diagrams in Figures 4.19 and 4.20. The bias is fixed to 100 mA.
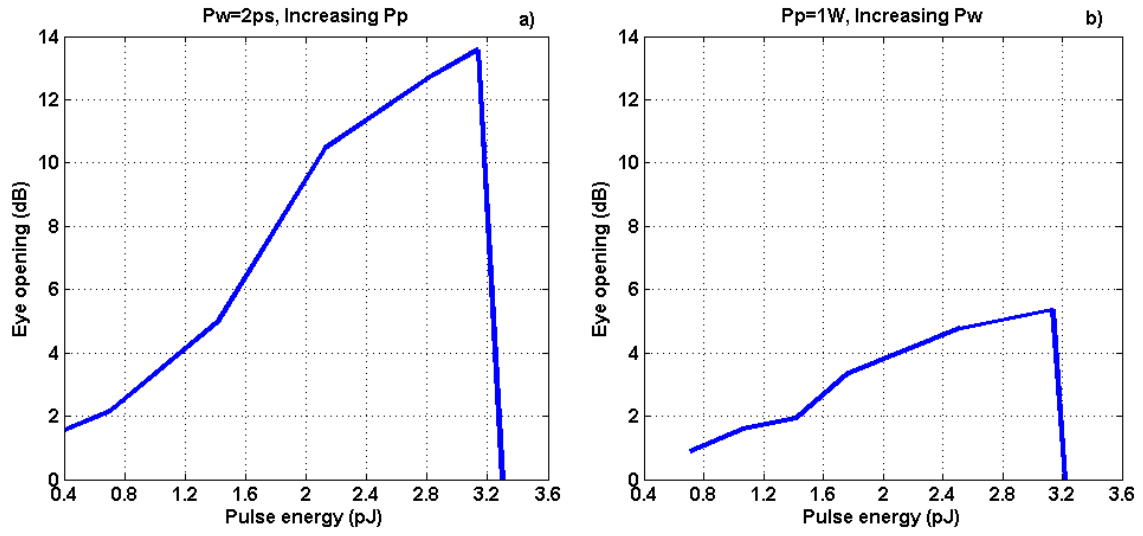
Figure 4.18: Eye opening vs pulse energy for a 10 Gb/s signal a) pulses with a 2ps width and increasing peak power. b) pulses with a 1W peak value and increasing width
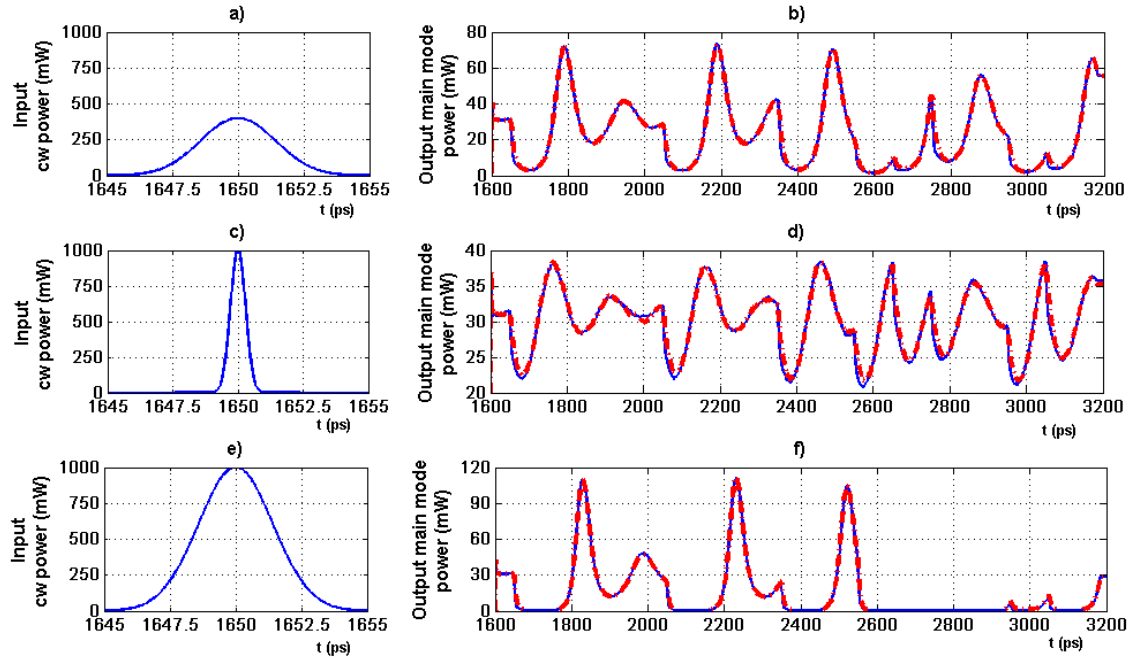

Figure 4.19: Time domain examples of the dynamic response to an external 10 Gb/s signal.

a) and b): input pulse example and output power in the case of 400 mW and 2 ps pulses.

c) and d): input pulse example and output power in the case of 1W and 0.4 ps pulses.

e) and f): input pulse example and output power in the case of 1W and 2 ps pulses.
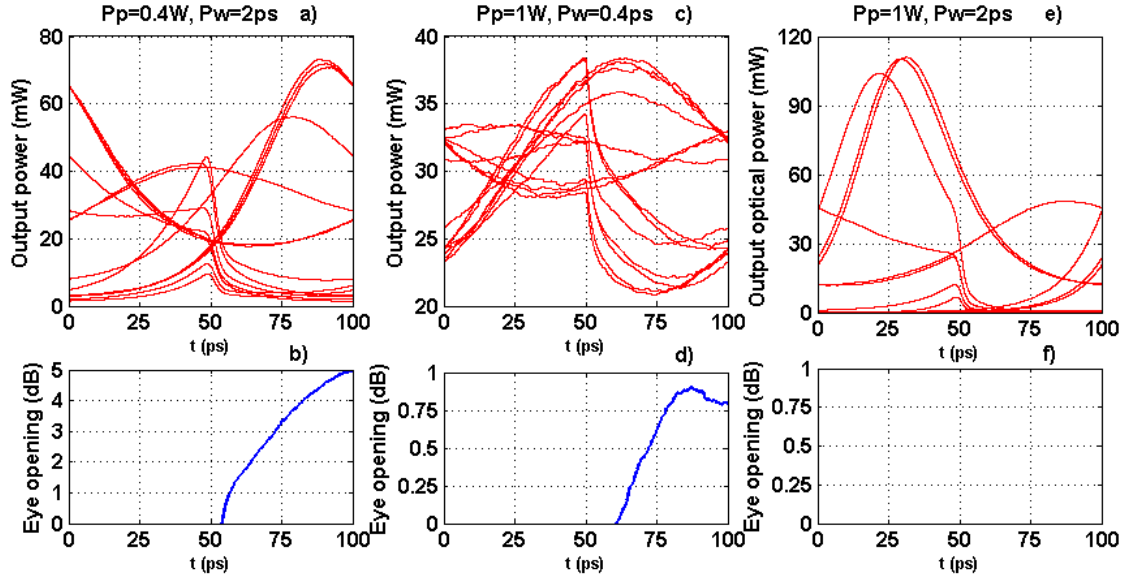
Figure 4.20: Eye diagram examples of the dynamic response to an external 2.5 Gb/s signal.

a) and b): Eye diagram and eye opening curve for 400 mW and 2 ps pulses.

c) and d): Eye diagram and eye opening curve for 1W and 0.4 ps pulses.

e) and f): Eye diagram and eye opening curve for 1W and 2 ps pulses.

It also becomes clear here the importance of carefully choosing a suitable pulse energy at such high bit-rates. If the pulse carries too much energy, the delay caused by the high overshoot or even laser shut-off becomes a major problem. Pulses over 3 pJ cause the recovery time to be too high and the eye opening falls drastically to negative values, as can be observed in Figure 4.19f and its corresponding eye opening Figure 4.20c.

4.3.3. Performance at 40 Gb/s

To finish this chapter, a test for 40 Gb/s is set. Once again the performance is checked for various bias current values. To have a fast recovery time, a pulse of about 2 pJ (with 400 mW of peak power and 2 ps width), not high enough to cause any turn-off or overshoot delay, is injected. The graph obtained is shown in Figure 4.21. Time-domain and eye-diagram examples are shown in Figures 4.22 and 4.23.
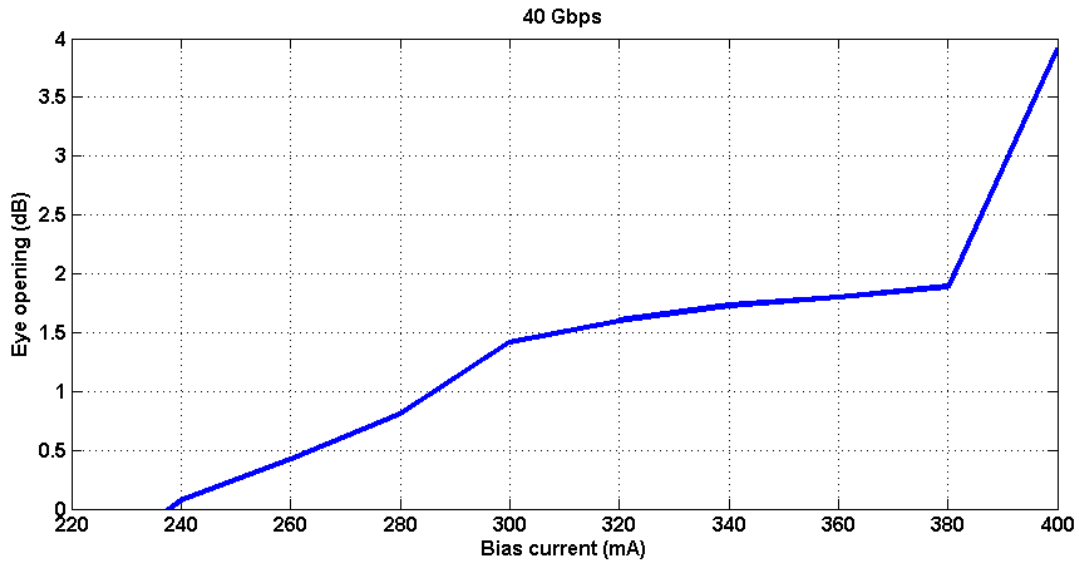
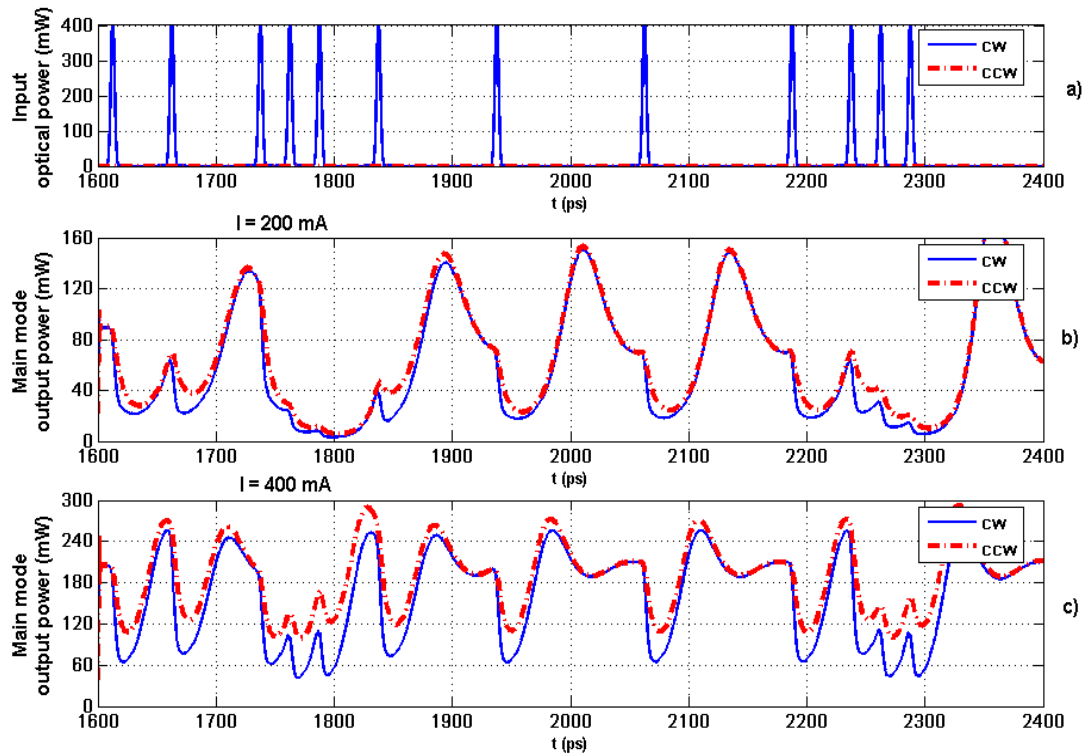*Figure 4.21. Eye opening vs bias current for a 40 Gb/s signal..*

Figure 4.22: Time domain examples of the dynamic response to an external 40 Gb/s signal. a) Input signals (equal for both cases). b) Output signal for I=200 mA. c) Output signal for I=400 mA.
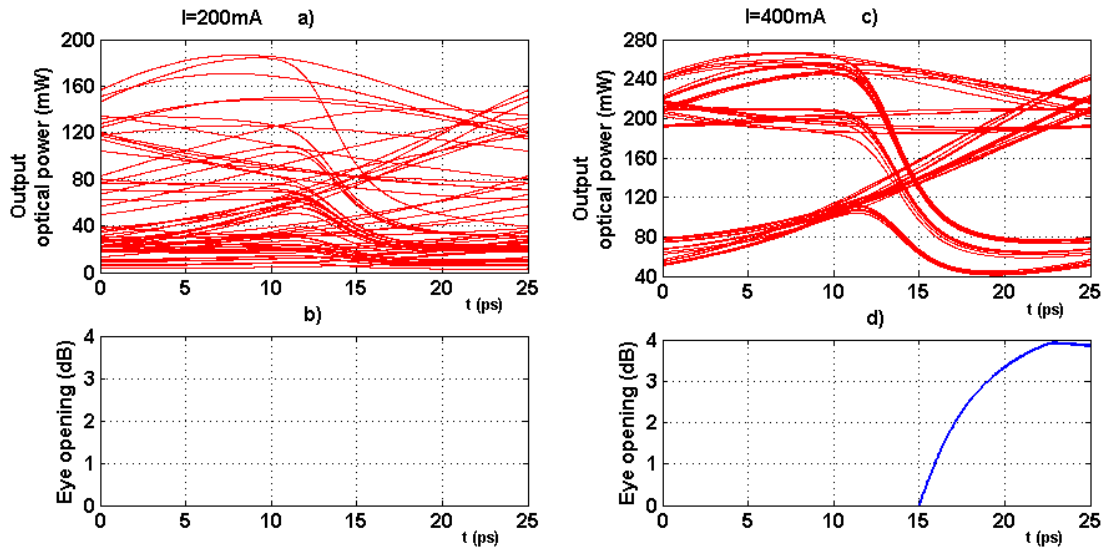
Figure 4.23: Eye diagram examples of the dynamic response to an external 40 Gb/s signal. a) and b): Eye diagram and eye opening curve for I=200mA. c) and d): Eye diagram and eye opening curve for I=400mA.

According to the results, operation at 40 Gb/s may be possible, but only if the bias is high enough for the relaxation oscillation frequency to reach the first maximum when the next pulse arrives. The eye opening only gets positive values for currents over 200 mA. Looking at the graph showed in Figure 4.4, this corresponds to a rise-time below 20 ps, which makes sense as the pulse repetition rate is 25 ps.

Operation in this scenario would not be possible if the pulses chosen have enough energy to cause laser shut-off or high overshoot, as the slightest delay would cause the eye-diagram to close completely.

Chapter 5

Conclusions and recommendations

In this thesis, a comprehensive numerical model to investigate micro-ring laser based all-optical signal processing applications has been developed. With this model, the response time of the laser to external injection of short pulses and the performance of the laser operating as a wavelength converter at different bit-rates was tested.

The model has been developed as close to the physical world as possible. It takes into account both inter- and intra-band ultra-fast carrier dynamics, such as two-photon absorption and free-carrier absorption, which model physical effects such as spectral-hole burning and carrier heating. These phenomena become increasingly important when the optical pulse duration is in the picosecond and sub-picosecond scale. The model effectively solves the field equations for the entire available spectrum, as a broadband noise with stochastic nature has been implemented. Therefore, it is unnecessary to previously calculate the allowed frequencies, which directly arise when the ring laser boundary conditions are applied. A simple gain dispersion model was added to the model, to control the optical bandwidth and to introduce the wavelength selectivity of real devices. Although no experimental data is available for such small ring lasers, the simulated results agree qualitatively well with experimental results for larger ring lasers.

The main objective of the thesis has been to evaluate if the recovery time of the micro-ring laser is fast enough for high-speed signal processing and if it could beat alternative SOA-based devices. This was done studying the performance of the device operating as a wavelength converter, where short Gaussian pulses were injected at the first resonant frequency, modulating the output at the main mode frequency.

The results show that even with small cavity length (30 μm) and under the injection of short pulses (0.2 to 10 ps) the relaxation oscillation frequency severely limits the performance of the device for high bit-rate signal processing applications (10 Gb/s and over). It was also observed that increasing the bias current can improve the performance of the device, but only to a certain limit. The relationship between relaxation frequency

and bias current follows a square root law, and that way to cut the rise-time by half, the bias current must be multiplied by four. In this sense, for operation at high bit-rates, the device must be pumped with high electrical injection, which comes out as a serious drawback, as low power consumption was one of the advantages foreseen in micro-ring lasers.

Also the effect of the injected pulses energies on the device performance was tested. Results show that for greater energies greater gain saturation is achieved and the eye opening becomes wider. Notwithstanding, if the pulse energy is too high complete saturation was reached and the laser shut-off, resulting in long delay-times as the mode had to be built up from noise again. Therefore great care must be taken when choosing the pulse energy. In order to achieve an optimum eye opening, a compromise must be set between level of gain saturation and recovery delay.

For future work, comparison with experimental data from micro-ring lasers is advised, in order to fine-tune the simulator parameters and validate the model. Also, as has been achieved in SOAs, the system performance might be improved by indirect approaches such as external filtering, a possibility that should be investigated and can be readily tested using the existing model.

The model should also be upgraded to model the asymmetries existing in real devices which might be responsible for the bistability characteristics of ring-lasers seen in experimental research, currently non-existent in this model. This way their nature and effects may be better understood if an asymmetry factor was added to the model.

Finally, the model developed include all the rich ultra-fast gain-dynamics shown by semiconductor materials and it may be used to study many more applications of these devices apart from wavelength conversion.

References

[1].   A. Odlyzko, *proceedings of the SPIE - Optical Transmission Systems and Equipment WDM II,* 2003, 5247, p. 1

[2].   D. Keck, "Optical fiber spans 30 years", *Lightwave*, 2000, 17 (8), p. 78.

[3].   R. Ramaswami and K. Sivarajan, *Optical networks: A practical perspective.* UK: Morgan Kaufmann Publishers, 1998.

[4].   CISCO, "Cisco CRS-1 MultiShelf System Data Sheet," 2006.

[5].   S. Yoo, "Optical packet and burst switching technologies for the future photonic internet", *IEEE/OSA J. Lightwave Techno*l., vol. 24, pp. 4468-4492, 2006.

[6].   H. Dorren, M. Hill, Y. Liu, N. Calabretta, A. Srivatsa, F. Huijskens H. Waart, and G. Khoe. "Optical packet switching and buffering by using all-optical signal processing methods," *IEEE/OSA J. Lightwave Technol.*, vol. 21, pp. 2-12, 2003.

[7].   M. Smit, "Photonic Integration" *Telektronikk* 2, 2005, p. 66.

[8].   http://www.infinera.com/technology/pic/largescale.html

[9]   S. Chuang, *Physics of Optoelectronic Devices*. Chichester: Wiley-Interscience, 1995.

[10].   A. Poustie, "SOA-based All-optical Processing", *Tutorial-OFC-2007*, Centre for Integrated Photonics, Ipswich, U.K. 2007.

[11].   H. Dorren, H. Mulvad, M. Hill, H. Waardt, A. Koonen, G. Khoe, J. Herrera Llorente, O. Raz, E. Tangdiongga, Y. Liu, J. Marti, F.Ramos, G. Maxwell and A. Poustie, "All-optical devices for ultrafast packet switching". *20th Annual Meeting of the IEEE Lasers and Electro-Optics Society (ThE5)*, Lake Buena Vista, Florida, 2007, pp. 729-730.

[12].   J. Marti, A. Koonen, H. Dorren, R. Caenegem, D. Colle, M. Pickavet, P. Demeester, E. Kehayas, L. Stampoulidis, D. Tsiokos, P. Bakopoulos, F. Ramos, H. Avramopoulos, J. Martinez, et. al. "IST-LASAGNE: All-optical label swapping employing optical logic gates and optical flip-flops", *proc. BroadBand Europe meeting, Paper T03A.01*, Bordeaux, France, 2005, pp. 1-6.

[13].   Z. Li, J. Mork, J. Molina, G. Khoe, H. Dorren and D. Lenstra, "Carrier heating from holes in the valence band in a bulk SOA", *proc. IEEE/LEOS Annual Meeting 06, ME1*, Montreal, Canada, 2006, pp. 50-51.

[14].   Z. Li, Y. Liu, J. Molina, E. Tangdiongga, S. Zhang, G. Khoe, H. Dorren and D. Lenstra, "Towards Terabit/s wavelength conversion with a single semiconductor optical amplifier and an optical bandpass filter", COBRA Research Institute, Eindhoven, The Netherlands, 2007.

[15].   Y. Liu, E. Tangdiongga, Z. Li, S. Zhang, H. Waardt, G. Khoe and H. Dorren, "Error-free all-optical wavelength conversion at 160 Gbit/s using a semiconductor optical amplifier and an optical bandpass filter", *J. Lightwave Technol.* 24, nr. 1, 2006, pp. 230-236.

[16].   Y. Liu, E. Tangdiongga, Z. Li, H. Waardt, A. Koonen, X. Shu, I. Bennion, G. Khoe and H. Dorren, "Error-free 320 Gb/s all-optical wavelength conversion using single semiconductor optical amplifier", *J. Lightwave Technol.* 25, nr. 1, 2007, pp. 103-108.

[17].   J. Herrera, H. Waardt, G. Khoe, A. Koonen, H. Dorren, E. Tangdiongga, Y. Liu, M. Hill, R. McDougall, A. Poustie, G. Maxwell, F. Ramos and J. Marti, "160-Gb/s all-optical packet-switching with in-band filter-based label extraction and a hybrid-integrated optical flip-flop". I*EEE Photonics Technol. Lett.* 19, nr. 13, 2007, pp. 990-992.

[18].   H. Dorren, M. Hill, Y. Liu, H. Ju, E. Tangdiongga, M. Smit and G. Khoe, "Digital Optical Singal Processing for Telecommunication Applications" *ICTON*, 2005, paper We.B1.1

[19].   M. Hill, M. Smit, H. Dorren, T. Vries, X. Leijtens, J. Besten, E. Smalbrugge, Y. Oei, J. Binsma and G. Khoe, "A fast low-power optical memory based on coupled micro-ring lasers". *Nature* 432, nr. 7014, 2004, pp. 206-209.

[20].   O. Raz, H. Dorren, S. Beri, Y. Barbarin, E. Bente, S. Anantathanasarn, and R. Notzel, "Non inverting and non filtered wavelength converter based on an InAs/InP QD ring laser at 1.55um", *OFC/NFOEC 2008* (pp. OWE5). San Diego, CA, 2008.

[21].   N. Calabretta, S. Beri, R. Notzel, E. Bente, J. Danckaert, M. Smit and H. Dorren."Regimes of operations of semiconductor ring lasers under optical injection and applications to optical signal processing", CLEO 2008 conference, pp. 1-2, 2008.

[22].   M. Connelly, *Semiconductor optical amplifiers*. Springer, 2001.

[23].   H. Haug and S. W. Koch, *Quantum Theory of the Optical and Electronic Properties of Semiconductors*. Singapore: World Scientific, 1994.

[24].   G. Agrawal and N. Dutta, *Long-Wavelength semiconductor lasers,* AT&T Bell Laboratories. Murray Hill, New Jersey, 1986.

[25].   G. Agrawal and N. Dutta, S*emiconductor lasers,* Springer, 1993.

[26].   J.Mark and J. Mørk, "Subpicosecond gain dynamics in InGaAsP optical amplifiers: Experiment and theory", *Appl. Phys. Lett.*, vol. 61, pp. 2281-2283, 1992.

[27].   J. Mørk, J. Mark and C. Seltzer, "Carrier heating in InGaAsP laser amplifiers due to two-photon absorption", *Appl. Phys. Lett.*, vol. 64, pp. 2206-2208, 1994.

[28].   M. Summerfield and R. Tucker, "Frequency-domain model of multiwave mixing in bulk semiconductor optical amplifiers", *IEEE J. Select. Topics Quantum Electron.*, vol. 5(3), pp. 839-850, 1999.

[29].   I. Stamataki, S. Mikroulis, A. Kapsalis and D. Syvridis, "Investigation on the Multimode dynamics of InGaAsP-InP Microring lasers", *IEEE J. Quantum Electron.*, vol. 42(12), pp.1266-1273, 2006.

[30].   J. Matanza, "DBR laser model and implementation", *Tech. Univ. Eindhoven, OED,* Eindhoven, The Netherlands, 2008.

[31].   M. Hill et al., "InAs-InP(1.55-μm Region) Quantum-Dot Microring Lasers", *IEEE Photon. Technol. Lett.*, vol. 20(6), pp. 446-448, 2008.

[32].   G. Agrawal, "Effect of gain dispersion on ultrashort pulse amplification in semiconductor laser amplifiers", *IEEE J. Quantum Electron.*, vol. 27(6), pp. 1843-1849, 1991.

[33].   A. Mecozzi and J. Mørk, "Saturation effects in nondegenerate four-wave mixing between short optical pulses in semiconductor laser amplifiers", *IEEE J. Select. Topics Quantum Electron.*, vol. 3(5), pp. 1190-1207, 1997.

[34].   R. Hamming, *Numerical methods for scientists and engineers*. London: McGraw-Hill, 1973.

[35].   X. Humet, F. Mestres, and J. Millan, "An analytical approximation for the Fermi-Dirac integral $f_{3/2}(\eta)$", *Solid-state electronics*, vol. 24(10), pp. 981-982, 1981.

Acknowledgments

I would like to thank the Electro-Optical Communications group of the Eindhoven University of Technology for giving me the opportunity to develop my Master thesis within the activities of the group in the last ten months.

Special thanks to Javier, my thesis supervisor, who has been a source for knowledge, patience and support. Thank you for all your help, tips, feedback and making the beginnings easy.

I also want to thank Harm Dorren, Ignacio de Miguel and Eduward Tangdiongga in granting me this great opportunity of experiencing one year in a foreign University and realizing my thesis within the optical communications field. I would like to stress the help received from Harm and Ignacio in my obtaining the Vulcanus scholarship, with which I will be enjoying a 12 month stay working with NTT corp. in Japan.

In the personal field, I am really grateful to my parents and to my brother for their unyielding support and understanding and to my close friends in Valladolid for their unconditional and true friendship.

Finally I would also like to mention all the new people I have met in Eindhoven which have made of this year a experience I will always remember.